Nanophotonic AFM Transducers Enable Chemical Composition and Thermal Conductivity Measurements at the Nanoscale

AUTHOR NAMES

Jungseok Chae,[1,2][†][‡] Sangmin An,[1,2][§][‡] Georg Ramer,[1,2] Vitalie Stavila,[3] Glenn Holland,[1] Yohan Yoon,[1,2] A. Alec Talin,[3] Mark Allendorf,[3] Vladimir A. Aksyuk[1]* and Andrea Centrone[1]*

AUTHOR ADDRESS

[1] Center for Nanoscale Science and Technology, National Institute of Standards and Technology, Gaithersburg, MD 20899, USA.

[2] Maryland Nanocenter, University of Maryland, College Park, MD 20742 USA

[3] Sandia National Laboratories, Livermore, CA 94551.

ABSTRACT

The atomic force microscope (AFM) offers a rich observation window on the nanoscale, yet many dynamic phenomena are too fast and too weak for direct AFM detection. Integrated cavity-optomechanics is revolutionizing micromechanical sensing; however, it has not yet impacted AFM. Here, we make a groundbreaking advance by fabricating picogram-scale probes integrated with photonic resonators, to realize functional AFM detection that achieve high temporal resolution (< 10 ns) and picometer vertical displacement uncertainty, simultaneously. The ability to capture fast events with high precision is leveraged to measure the thermal conductivity (η), for the first time, concurrently with chemical composition at the nanoscale in photothermal induced resonance experiments. The intrinsic η of metal-organic-framework individual microcrystals, not measurable by macroscale techniques, is obtained with a small measurement uncertainty (8 %). The improved sensitivity (50×) increases the measurement throughput 2500-fold and enables chemical composition measurement of molecular-monolayer-thin samples. Our paradigm-shifting photonic readout for small probes breaks the common tradeoff between AFM measurement precision and ability to capture transient events, thus transforming the ability to observe nanoscale dynamics in materials.

KEYWORDS

Table of Content graphic
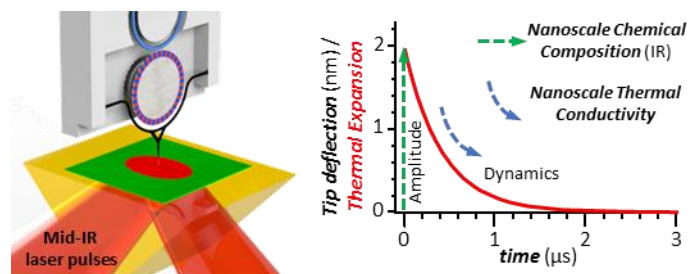
TEXT

The atomic force microscope (AFM) enables progress in material science,[1, 2] biology,[3] and other fields, by detecting morphological, chemical,[4, 5] mechanical,[3, 6] thermal,[7, 8] electrical,[9] optical,[10] and other properties with nanoscale resolution. Considerable efforts are directed towards improving AFM detection bandwidth and sensitivity to increase throughput, the ability to detect small signals, and to capture dynamic events such as protein folding[3], heat diffusion[11] and others[6] at progressively shorter time scales. Reduction of the probe mass enables faster response and widens the detection bandwidth; reduction of size lowers dissipation and force noise from fluid drag. However, because far-field optical detection becomes inefficient for probes with cross-sections below the diffraction limit,[12] rapid and low-noise motion detection for very small probes is challenging and curbs the benefits of probe miniaturization. Cavity-optomechanics is revolutionizing micromechanical sensing[13-15] in many applications, and has been proposed for realizing an AFM sensor.[15] However high-performance AFM measurements based on cavity-optomechanics have not been demonstrated, until now, due to the serious microfabrication challenges that must be overcome to transition from simplified demonstrative devices[15] to fully-integrated, functional AFM probes.

Leveraging dynamic signal detection, photothermal induced resonance (PTIR)[2, 4, 5, 16] combines the spatial resolution of AFM with the specificity of absorption spectroscopy (Fig. 1A). In PTIR, when the sample absorbs a light pulse it heats up and expands inducing vibrations in the AFM cantilever (like a struck tuning fork) with amplitudes directly proportional to the absorption coefficient of the sample.[17] Notably, the proportionality of the PTIR signal to the energy absorbed by the sample,[17, 18] as in conventional infrared (IR) spectroscopy, allows material identification by comparison with far-field IR spectral databases.[16] PTIR also enables conformational analysis[4], mapping of composition[19], and bandgap[20] at the nanoscale. Although conventional cantilevers adequately capture the light absorption magnitude, they lack the speed and motion-detection precision for tracking the sample thermal expansion dynamics to extract its local thermal conductivity (η).[11]

In this work, an integrated near-field cavity-optomechanics readout concept[15] is implemented, for the first time, to realize fully-functional nanoscale AFM probes capable of ultralow detection noise (≈ 3 fm·Hz$^{-0.5}$) within an extremely wide measurement bandwidth (> 25 MHz) in ambient conditions, surpassing all previous AFM probes. This advance allows capturing previously inaccessible PTIR time-domain thermal expansion dynamics with high temporal resolution (<10 ns) and low noise (<1 pm per point), while simultaneously improving the PTIR signal-to-noise ratio (*SNR*). The low probe mass yields high quality nanoscale IR spectra even from thin (< 2 nm) samples. The high temporal resolution ($\approx 1500\times$-faster than temperature-sensitive probes, see supplemental discussion – SD 1)[11] enables accurate evaluation of the thermal conductivity from samples that are too small, heterogeneous at the nano-scale and/or difficult to prepare for micro- and macro-scale techniques.[21] This new method is validated by analyzing polymethyl-methacrylate (PMMA) thin films with well-known characteristics, and later applied to measure the

thermal conductivity of metal-organic framework (MOF)[22, 23] microcrystals of unknown η. MOFs are a class of nanoporous materials promising in catalysis, gas storage, sensing and separations. Accurate knowledge of the thermal conductivity is crucial to engineering MOFs for these applications, and for novel MOF-based thermoelectric devices; however, η has been measured only for a few MOFs.[24, 25] Because these materials are typically obtained as microcrystalline powders, macroscale thermal conductivity measurements are affected by the crystals packing density and do not provide the intrinsic η. The development of an ultrasensitive near-field optical motion readout of a fast and ultralight (≈ 1.2 pg) AFM transducer probe is the key revolutionary advance that allows measurement of the intrinsic thermal conductivity of MOFs crystals presented here, and of other nanomaterials.

Here, a fiber-pigtailed optomechanical transducer chip (hereafter transducer), was integrated into a modified commercial PTIR setup[26] using a custom 3D-printed adaptor, replacing the conventional AFM cantilever. The transducer (Fig. 1C,E), consists of a picogram-scale mechanical probe wrapped around a stationary microdisk optical resonator cavity implementing high quality-factor (Q) interferometric motion readout. The nominally 100 nm to 200 nm wide, 20 µm long mechanical probe and 10 µm diameter microdisk were nanofabricated from a ≈ 260-nm thick single-crystal Si layer (details available in the supporting information, SI). A 500-nm-wide on-chip Si waveguide is evanescently coupled to the cavity, and connected via optical fibers to a continuous-wave tunable laser (1520 nm – 1570 nm) and to a photoreceiver, replacing the AFM laser beam-bounce detection (Fig 1C). The evanescent fields of the disk whispering-gallery optical modes provide optomechanical coupling between the probe and the disk across a small air-gap (≈ 150 nm). Each of the disk's optical resonances ($15000 < Q < 100000$) manifests as a dip in the transducer's transmission spectrum (see Fig 1F), and shifts sharply and

proportionally to the probe displacement (typical optomechanical coupling $g_{OM}/2\pi \approx 0.5$ GHz/nm). In operation, the laser wavelength is fixed at the steepest slope point on the resonance side such that probe motion modulates the transmitted light intensity, yielding the AFM "*deflection signal*".

In PTIR, a wavelength-tunable pulsed (≈ 10 ns) laser illuminates the sample and an AFM tip contacting the sample serves as local detector (Fig 1A,C). The absorbed (mid-IR) light excites vibrational modes localized on specific chemical groups, converting optical energy into vibrational energy. Within < 1 ns, the vibrational energy is redistributed to lower-energy modes and transferred to phonons, which transport the heat.[26] The consequent rapid sample thermal expansion displaces the AFM tip and excites one or more cantilever oscillation modes. The probe motion is measured by reflecting a laser beam off a conventional cantilever towards a position-sensitive detector (Fig 1A) or by measuring the transmitted-light intensity using the transducers (Fig 1C). In our setup, the photodetector output from the transducer is digitized with a fast oscilloscope (500 MHz sampling rate) to capture the time-domain PTIR signal with high temporal resolution. The oscilloscope traces were saved and analyzed offline to gain access to the sample thermal expansion dynamics (see below). Simultaneously, the same signal, buffered by the oscilloscope preamplifier, was fed into the commercial PTIR system where it was separately digitized (50 MHz sampling rate). To reduce the noise introduced by the commercial digitizer the signal was filtered by a broad band-pass FFT filter (≈ 3.7 MHz bandwidth) around the transducer resonant frequency (≈ 10 MHz). IR spectra and maps were generated by the commercial PTIR software that determines the peak-to-peak amplitude (maximum minus minimum intensity) of the filtered PTIR time-domain signal trace; which is proportional to the absorbed energy.[17, 18] When using conventional cantilevers the FFT filter had a bandwidth of 100 kHz centered at the cantilever second mechanical resonance (≈ 200 kHz).

Fig 2A-C shows the topography, PTIR maps and spectra obtained using the transducer on a chemically heterogeneous polymer sample demonstrating chemical imaging with high spatial resolution, similarly to previous PTIR experiments using conventional cantilevers.[18]

Generally, the PTIR signal (S) is a sum of up to 3 terms:

$$(1) \qquad\qquad S = S_{osc} + S_{exp} + S_{bkg}.$$

Here S_{osc} describes the ring-down dynamics of the cantilever mechanical oscillations. For a fast probe, S_{exp} additionally describes the probe's motion, tracking directly the fast sample thermal expansion and slower contraction. S_{bkg} describes any contribution to the output signal that is not mechanical in nature (background). S_{osc} is the only measurable signal with conventional cantilevers (Fig 1B) or with the transducers on samples with fast thermalization dynamics (Fig 2D). Only the first transducer contact-mode (≈ 10 MHz, Fig. 1G) contributes to S_{osc}, because the faster, higher-order modes adiabatically follow the ≈ 10 ns sample thermal expansion.

The transducers allow measuring PTIR spectra of a ≈ 2 nm thick Octadecylchlorosilane (OTS) monolayer (Fig. 2E, fig S1) with high SNR (≈ 174) and in good agreement with macroscale FTIR spectra.[27] Remarkably, although OTS has only one CH_3 group per molecule, its spectrum clearly shows the CH_3 antisymmetric-stretching peak (2962 cm^{-1}). For such a thin sample, the laser pulse and the sample thermalization (< 1 ns), are much faster than the oscillation period for either the transducer (≈ 10 MHz) or a conventional cantilever (≈ 200 kHz) contact modes frequencies. Because in this regime the oscillation amplitude excited by the impulsive sample expansion is proportional to the mode's resonance frequency (see supplemental discussion SD-2), the transducers provide $\approx 50\times$-larger mechanical amplitude. For a sufficiently low-noise motion readout, such as in the case of our transducers (Figure 1G), the measurement SNR is determined by the cantilever amplitude response relative to the cantilever thermal motion noise ($<x^2> = K_B T/k$

per equipartition theorem, where K_B is the Boltzmann constant, T is the temperature, k is the cantilever stiffness and x is the cantilever motion). Because conventional cantilevers and the transducers have comparable stiffness, the larger signal amplitude of the transducers results in a 50x-larger *SNR* (Fig. 1D) than for conventional cantilevers (Fig 1B) when measuring the same sample (i.e. 50 nm thick PMMA in Fig. 1) under identical experimental conditions (sample location power, polarization, wavelength, averages).

Using conventional cantilevers, an additional Q-fold mechanical gain is obtained with the resonance-enhanced PTIR technique,[5] by resonantly exciting a cantilever mode at the resonance frequency f. In contrast, the transducer's high gain is intrinsic, that is independent of Q and f (or weakly dependent on f near resonance in the case of samples with short-lived thermal expansion, see SD-2). Therefore, the transducer PTIR measurement is largely immune to possible artefacts induced by modest changes in f and Q due to spatially-varying stiffness and damping at the probe-sample contact point.

In PTIR, the measurement uncertainty is determined by the sum of the probe and optical readout input-referred displacement noise power. Reduction of the probe's cross-section to the nanoscale strongly reduces air-drag and the corresponding thermodynamic force noise-spectral-density, which lowers the displacement noise-density at all frequencies away from the probe resonance. The input-referred noise of the optomechanical readout is not only much smaller than the displacement noise near the resonance, but more importantly, it approaches the probe displacement noise *at all frequencies below resonance* (Fig. 1D, see SD-3). The large bandwidth and low noise of our transducers are ideal for directly measuring fast time-domain sample surface motion (Fig. 3).

The thermal-expansion dynamics of the sample surface is influenced by the η which governs the heat diffusion within the sample. Consequently, the local η can be extracted from the S_{exp} term of the PTIR signal, leveraging a suitable thermo-mechanical model. Thermoreflectance experiments[21] that also evaluate η by measuring surface motion, typically rely upon finite-element method calculations of the heat diffusion in the sample and substrate. However, we find (see SD-4) that for an impulsive excitation and for a substrate with high thermal conductivity (i.e. heat-sink at constant temperature) the sample temperature and thermal expansion are well described by an instantaneous rise followed by a single exponential relaxation $\propto e^{-t/\tau_s}$, where τ_s is the time constant of the slowest (fundamental) thermal mode. This simplified, yet acceptably accurate model enables analytical calculation of S_{exp}, thereby potentially allowing near real-time data analysis and η-mapping. Because the phonon mean free path in PMMA is below 1 nm,[28] and well below the sample thickness analyzed in this work, no ballistic heat transport is considered in our model.

With these assumptions, the contributions to the PTIR signal are (see SD-5 and SD-6):

(2) $\quad S_{osc} = \dfrac{A \cdot e^{\frac{-\pi f t}{Q}}}{2\left[1+\left(\frac{1}{2\pi f \tau_s}-\frac{1}{2Q}\right)^2\right]} \cdot \left(-\cos(2\pi f t) + \left(\frac{1}{2\pi f \tau_s}-\frac{1}{2Q}\right) \cdot \sin(2\pi f t)\right)$

(3) $\quad S_{exp} = A \cdot \left[r - \dfrac{1}{2}\dfrac{\left(\frac{1}{2\pi f \tau_s}-\frac{1}{2Q}\right)^2}{1+\left(\frac{1}{2\pi f \tau_s}-\frac{1}{2Q}\right)^2}\right] \cdot e^{-\frac{t}{\tau_s}}$

(4) $\quad S_{bkg} = B x_t \int_0^t \exp\left(-\dfrac{v}{\tau_s}\right)(t-v)^{-3/2}\exp\left(\dfrac{x_t^2}{4\alpha(t-v)}\right)dv$

where t is the time, τ_s is the sample thermalization time, A, f and Q are the amplitude, frequency and Q-factor of the probe oscillation mode, respectively. r is the ratio of DC to AC amplitudes of the optically read-out cantilever response to a step-function. S_{bkg} in our experiments (see SD-6) arises from non-local through-air heat transfer from the hot sample surface, which shifts the optical

resonance via the thermo-optic effect. Eq.4 describes the expected time-dependent air temperature change at distance x_t from the sample surface, whose temperature decays exponentially after a fast raise. If used as independently adjustable parameters, data fitting returns the expected values for the air thermal diffusivity (α) and surface-disk distance x_t. Similarly, the r from the fit agrees with an independent calculation from the probe parameters (see SD-5). Notably, S_{osc}, S_{bkg} and S_{exp} have different time scales (Fig. 3A,B) and are well separated in the frequency domain, facilitating the fit and a robust parameter estimation. S_{osc} is centered near the $\approx$ 10 MHz probe frequency ($\tau_{osc} = 1/(2\pi f) = 16$ ns), S_{exp} has a relaxation time 40 ns $< \tau_s <$ 1700 ns for the samples analyzed here, and the S_{bkg} peaks at about 2 µs.

In the absence of interfacial thermal resistance (R), τ_s is given by[11] (see SD-7):

$$(5) \qquad \tau_s = \frac{4}{\pi^2} \cdot \frac{C_p \cdot \rho \cdot z^2}{\eta} = \frac{4}{\pi^2} \cdot \frac{z^2}{D}$$

where C_p is the specific heat capacity, ρ is the density, $D = \eta/(C_p \cdot \rho)$ is the thermal diffusivity and z is the sample thickness. Measuring z and τ_s allows determination of the local D, or η, when C_p and ρ are known. For finite R, τ_s satisfies

$$(6) \qquad \begin{cases} \tau = \frac{C_p \rho}{\eta} l_0^2 \tan^2 \xi \\ l_0 \xi \tan \xi = z \end{cases}$$

where $l_0 \equiv \eta/R$ (SD-7). In the limit of small R, $l_0 \ll z$, $\xi \to \frac{\pi}{2}$, leading to eq. 5.

The τ_s values measured on a PMMA wedge sample (15 nm $< z <$ 600 nm) follow approximately the expected z^2-dependence (Fig 3C), while plotting $\eta_{eff}(z) \equiv \frac{4}{\pi^2} \cdot \frac{C_p \cdot \rho \cdot z^2}{\tau_s(z)}$ (Fig. 3D) qualitatively highlights the effect of the interfacial thermal resistance (for negligible R, η_{eff} would be z-independent). The τ_s uncertainty represents a single standard deviation of repeat measurements obtained on distinct locations of the same thickness and with different instrumental parameters

such as excitation wavelength and pulse energy. Leveraging known values for C_p and ρ (Table S1) and using η and R as adjustable parameters, an error-weighted implicit fit of (6), (fig 2C, D) yields $\eta = 0.178$ W·m^{-1}·K^{-1} $\pm$ 0.014 W·m^{-1}·K^{-1}. The acquisition-time per point (≈ 2 s) and the nanoscale η uncertainty (≈ 8 %) compare favorably with the acquisition time and uncertainty of state-of-the-art thermo-reflectance measurements [21, 29] with micron-scale spatial resolution.

Having validated our model on PMMA, we next measure HKUST-1[30] microcrystals (Fig 4) obtained directly on the ZnSe prism by adapting an ink-jet printing method[31]. The measured $\tau_s(z)$ values are well described by equation 5 (Fig 4C) and using HKUST-1 known C_p and ρ (table S1) we estimate $\eta^{HKUST-1} = 0.26$ W·m^{-1}·K^{-1} $\pm$ 0.02 W·m^{-1}·K^{-1} at $RH = 1.8$ % $\pm$ 0.3 % (Fig. 4D). In contrast to steady-state measurements reporting a negative thermal-expansion coefficient for HKUST-1,[32] our technique directly measures a positive expansion at short time scales (< 1 µs). This new observation highlights the complexity of the thermo-mechanical behavior in these materials, and may foster a better understanding of their fundamental properties.

In summary, the very large bandwidth and SNR of the picogram cavity-optomechanical probes open AFM access to fast dynamic processes at the nanoscale. This advanced transduction technique enables detection of chemically-specific IR absorption of short laser pulses by monolayer-thick films in PTIR, increasing sensitivity by almost two orders of magnitude. Furthermore, it also provides direct access to fast sample thermalization dynamics in the time domain enabling concurrent measurements of chemical composition and thermal properties at the nanoscale. Because PTIR allows material identification, informing on ρ and C_p via literature data, we reason that this method can provide η for samples and impurities whose composition is initially unknown. While the 50× PTIR signal-to-noise ratio improvement decreases the need for averaging 2500-fold, the transducers also relax back to equilibrium after each pulse 100-times faster (≈ 5 µs,

Fig 1D) than conventional cantilevers (> 500 µs, Fig 1B) and leveraging high (200 kHz) repetition rate lasers[5], could further improve the PTIR throughput 200-fold (see SD-8).

Because many nanomaterials consist of nanoparticles or microcrystals that are too small or heterogeneous for macro-scale thermal conductivity measurements, we believe that the method presented here will foster the development of nanomaterials in thermoelectric, electronic and other applications. Furthermore, we believe that the transducers' low drag cross-section (see SD-3) will open new opportunities for nanoscale chemical imaging in liquids with a future broad impact in biology, medicine, and materials science.

PTIR SETUP AND MEASURMENTS

PTIR experiments were obtained using a modified commercial PTIR instrument. The set up used in this work consists of a contact mode atomic force microscope (AFM) interfaced with wavelength-tunable pulsed laser sources (laser A and B), as described previously.[33] Laser A consists of an optical parametric oscillator based on a noncritically phase-matched $ZnGeP_2$ crystal that emits 10 ns long pulses (≈ 10 cm^{-1} linewidth) at 1 kHz repetition rate in the spectral range from 4000 cm^{-1} to ≈ 1025 cm^{-1} (from 2.5 µm to 9.76 µm). Laser B consists of a synchronously pumped difference frequency generation laser system emitting ≈ 100 ps long pulses with a 0.5 cm^{-1} linewidth at 1 kHz repetition rate. Laser B wavelength is nominally tunable between 6450 cm^{-1} (1.55 µm) to 625 cm^{-1} (16.00 µm). Laser A and B emit linearly polarized light. Because the laser power at the sample was controlled with a wire grid polarizer, the light polarization at the sample is also affected by the polarizer's settings. In each experiment the light polarization at the sample was linearly polarized and constant, but the polarization state was not deliberately controlled and may have varied between experiments, unless otherwise noted.

Conventional PTIR measurements were obtained by reflecting the AFM laser beam off 450 μm long conventional Si contact-mode AFM probes (nominal spring constant between 0.07 N/m and 0.4 N/m) onto a 4-quadrant AFM detector (see Fig 1A).

PTIR measurements with the optomechanical transducers (see Fig 1C of the main text) were obtained by mounting the transducer chip on a custom AFM head using a 3D-printed stainless steel adaptor. The detection scheme (Fig 5) consists of a fiber coupled continuous wave (CW) tunable laser (1520 nm – 1570 nm), an optical isolator, a variable optical attenuator, a fiber polarization controller, the transducer and a room-temperature InGaAs photoreceiver (DC coupled, 3 dB bandwidth of 125 MHz).

The signal from the photoreceiver is used to provide both the vertical deflection signal for the AFM, and PTIR signal ($S = S_{osc} + S_{exp} + S_{bkg}$). To provide the AFM feedback, the signal is low pass filtered and amplified (1-fold to 5-fold) and then fed to the vertical deflection input channel of the commercial PTIR system. To record and analyze the fast thermal expansion dynamics of the sample, the photodetector output is digitized with a fast oscilloscope (11 bit) at a sampling rate of 500 MHz. Oscilloscope traces of the time-domain PTIR signal were saved and analyzed offline as described in the main text. The preamplifier circuit of the oscilloscope is also used to buffer the signal before feeding it to a fast input channel (50 MHz sampling rate) of the commercial PTIR system. This scheme allows to perform in depth offline analysis of the fast probe dynamics (oscilloscope traces) as well as to use the digitizing electronics, algorithms and software of the commercially available PTIR system for PTIR spectral acquisition and imaging. The PTIR spectra and maps were obtained using the commercial software of the PTIR instrument, recording the peak-to-peak amplitude of the oscillatory term (S_{osc}), which is proportional to the absorbed energy.[17, 18]

Spectra were obtained by averaging the response traces from 256 laser pulses at each wavelength and by sweeping the wavelength at 4 cm^{-1} intervals. PTIR images were recorded by illuminating the sample with a constant wavelength while scanning the sample. The *SNR* of the PTIR traces in Fig 1B and Fig 1D was obtained by dividing the PTIR peak to peak signal (maximum minus minimum intensity of the time-domain trace) by the peak to peak noise obtained after the completion of the cantilever ringdown. The AFM height and the PTIR signal acquisition was synchronized so that for each pixel the PTIR signal was an average over 32 laser pulses. The pixel sizes are 100 nm × 100 nm in all images.

The oscilloscope PTIR traces used to evaluate the sample thermal conductivity were obtained by averaging typically 2048 individual pulse responses, which provide a typical statistical uncertainty of < 1 pm per point when sampled at 10 ns per point (averaging 5 sequential points recorded at 500 MHz sampling rate), as detailed in supplemental discussion 3.
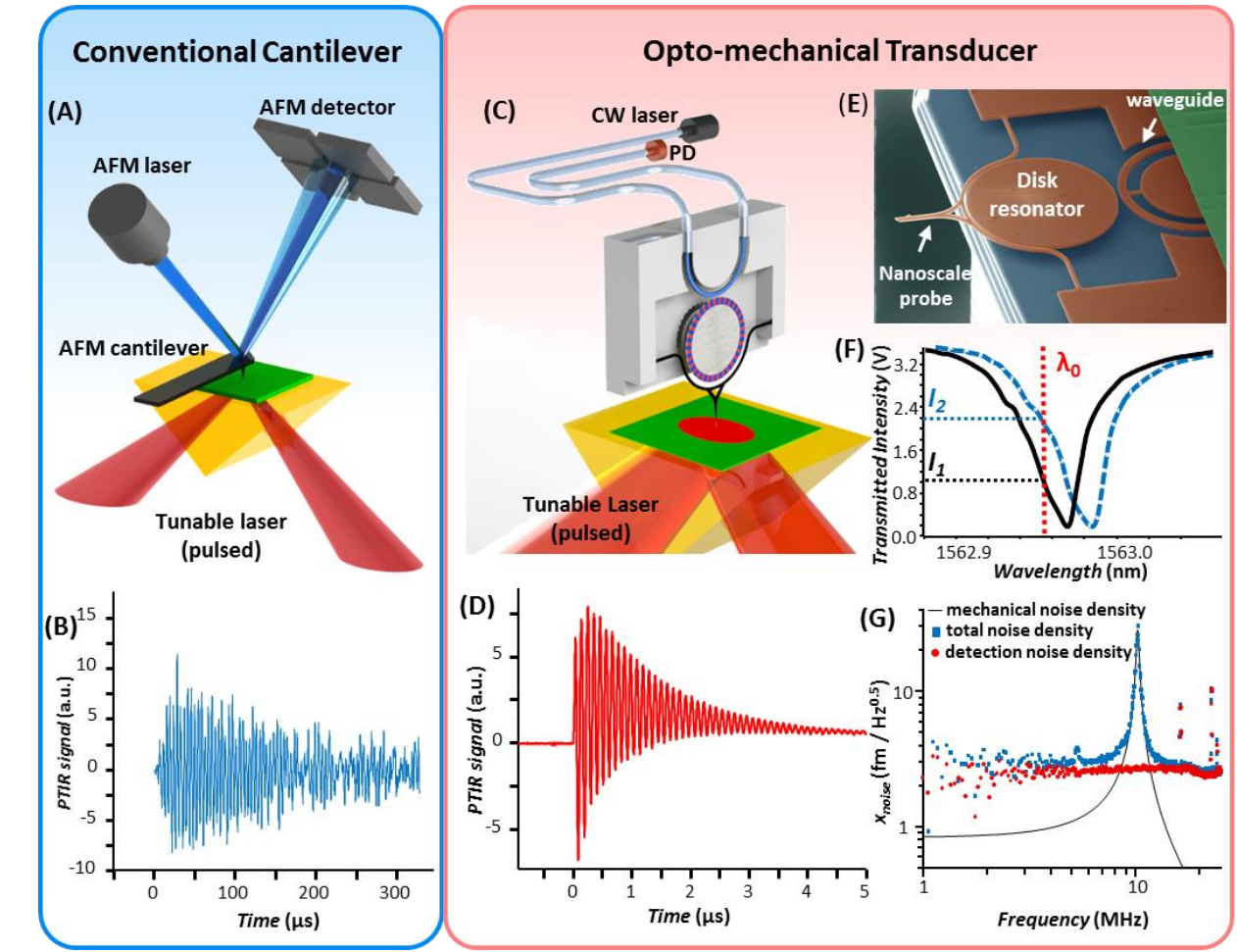
Fig. 1. **Nanophotonic optomechanical transducers enable large-bandwidth, low noise PTIR measurements.** (A) Conventional PTIR: a wavelength-tunable pulsed laser (red) excites the sample in total internal reflection. Following the absorption of a laser pulse, the sample rapidly expands and excites the oscillation modes of an AFM cantilever. The oscillation amplitude (peak to peak) is proportional to the absorbed energy, enabling nanoscale IR spectroscopy; however, the SNR and bandwidth of conventional AFM cantilevers are insufficient for capturing the fast sample thermal expansion and thermalization dynamics. (**B**) Conventional cantilever PTIR signal for a thin, 50 nm PMMA film. (**C**) Photonic transducer PTIR: a fiber-pigtailed, integrated transducer

leverages cavity-optomechanics to measure motion of a nanoscale probe, radically reducing the noise and increasing the measurement bandwidth for capturing the sample's fast thermalization dynamics induced by laser pulses. (**D**) The opto-mechanical transducer improves the PTIR *SNR* by $\approx$ 50 for a 50 nm PMMA film under the same conditions of panel B (1160 cm^{-1}, 256 pulses averaged). (**E**) Transducer's colorized scanning-electron micrograph: a nanoscale Si probe is near-field coupled across a nanoscale gap to high-*Q* whispering-gallery optical modes of a Si microdisk optical cavity. The cavity is evanescently coupled to an integrated waveguide. (**F**) During the measurement the fiber-coupled laser wavelength (λ_0) is fixed; the sample expansion reduces the cantilever-disk gap, shifting the resonance to longer wavelengths and increases the transmitted intensity (*I*) proportionally to the displacement. The measured spectrum before the laser pulse (black) is shifted 15 pm (blue), illustrating a sample thermal expansion of $\approx$ 3.75 nm. (**G**) The transducer provides an ultralow input-referred measurement noise spectral density (blue) across a wide (25 MHz) bandwidth; integrated over the full bandwidth, the probe thermodynamic noise (black line) slightly exceeds the detection noise (red). (see SD3).
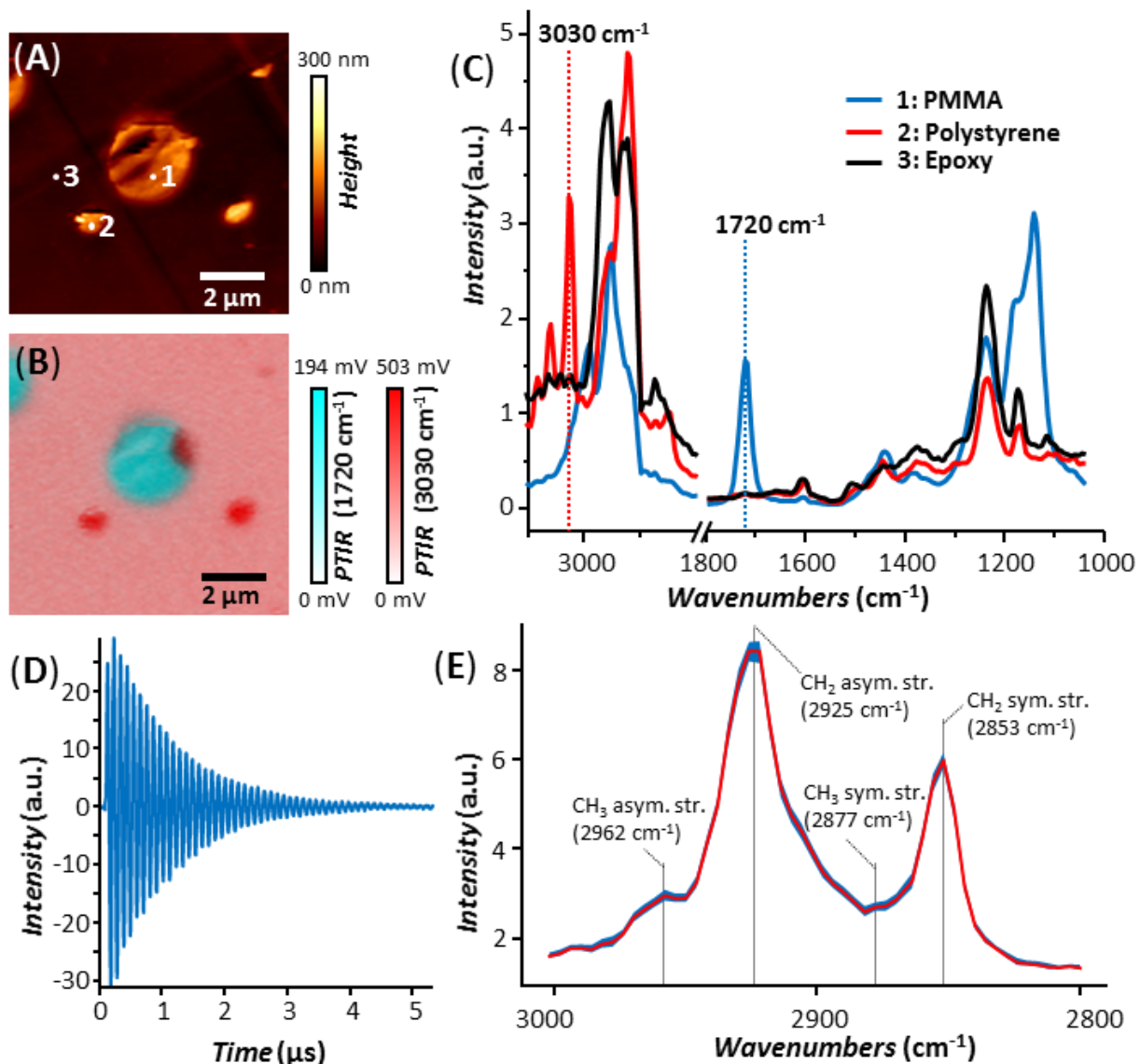
Fig. 2. The transducers enable IR spectroscopy and mapping with high sensitivity and resolution. (**A**) AFM topography and (**B**) PTIR (1720 cm^{-1}, 3030 cm^{-1}) composition overlay maps of a PMMA (light blue) and polystyrene (red) particles in epoxy matrix (pink). (**C**) PTIR spectra from marked positions in panel A. (**D**) PTIR transducer signal and (**E**) spectrum of an OTS monolayer. The red trace and blue shaded-area are the average of 12-spectra from different sample locations and its 95 % confidence uncertainty. Because of the fast OTS thermalization $S \approx S_{osc}$.
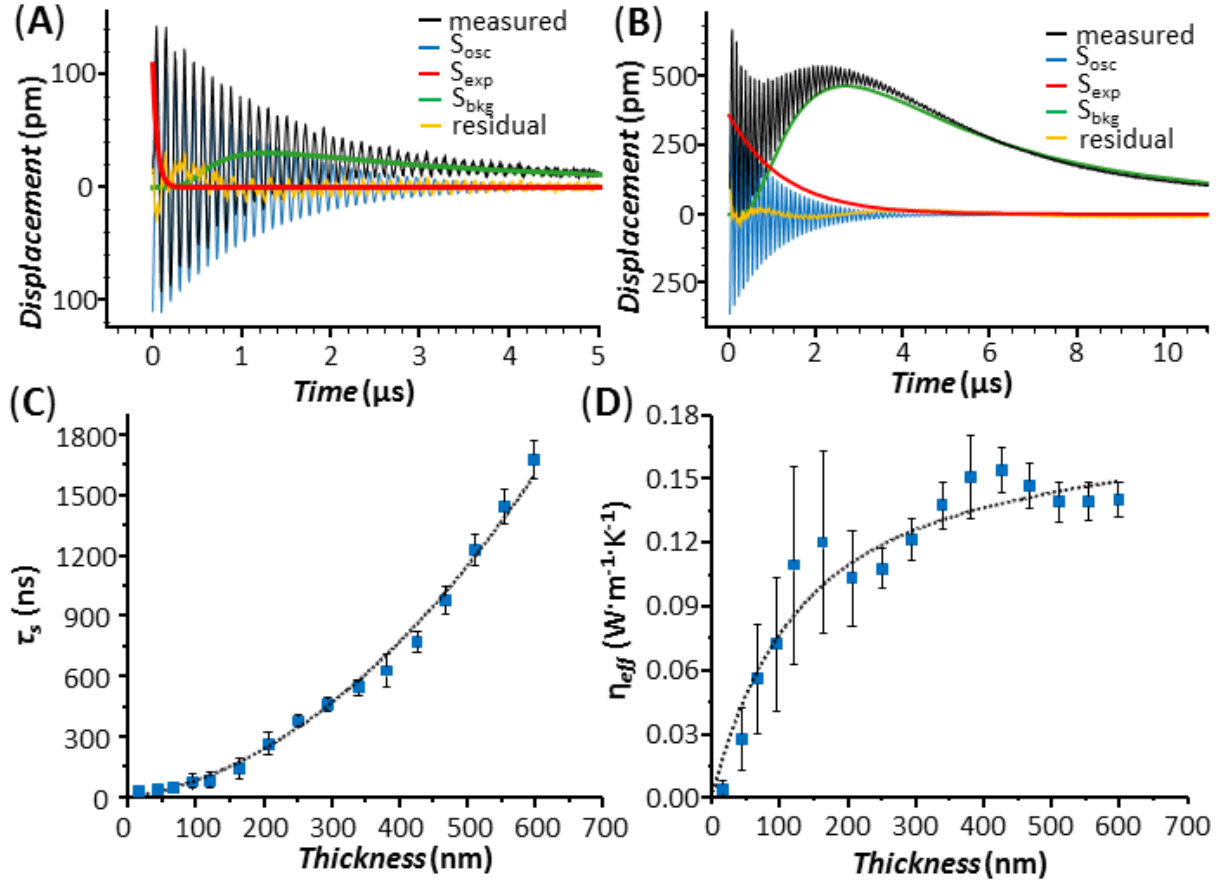
Fig. 3. The transducers enable measuring PMMA thermal conductivity. (**A**) Transducer signal (1236 cm^{-1}) for 66 nm thick and (**B**) 598 nm thick PMMA. (**C**) PMMA thermalization time as a function of thickness; the black line is the best fit given by Eq. 6. (**D**) PMMA effective thermal conductivity (η_{eff}) as a function of thickness, line based on the Eq. 6 fit to measured τ_s.

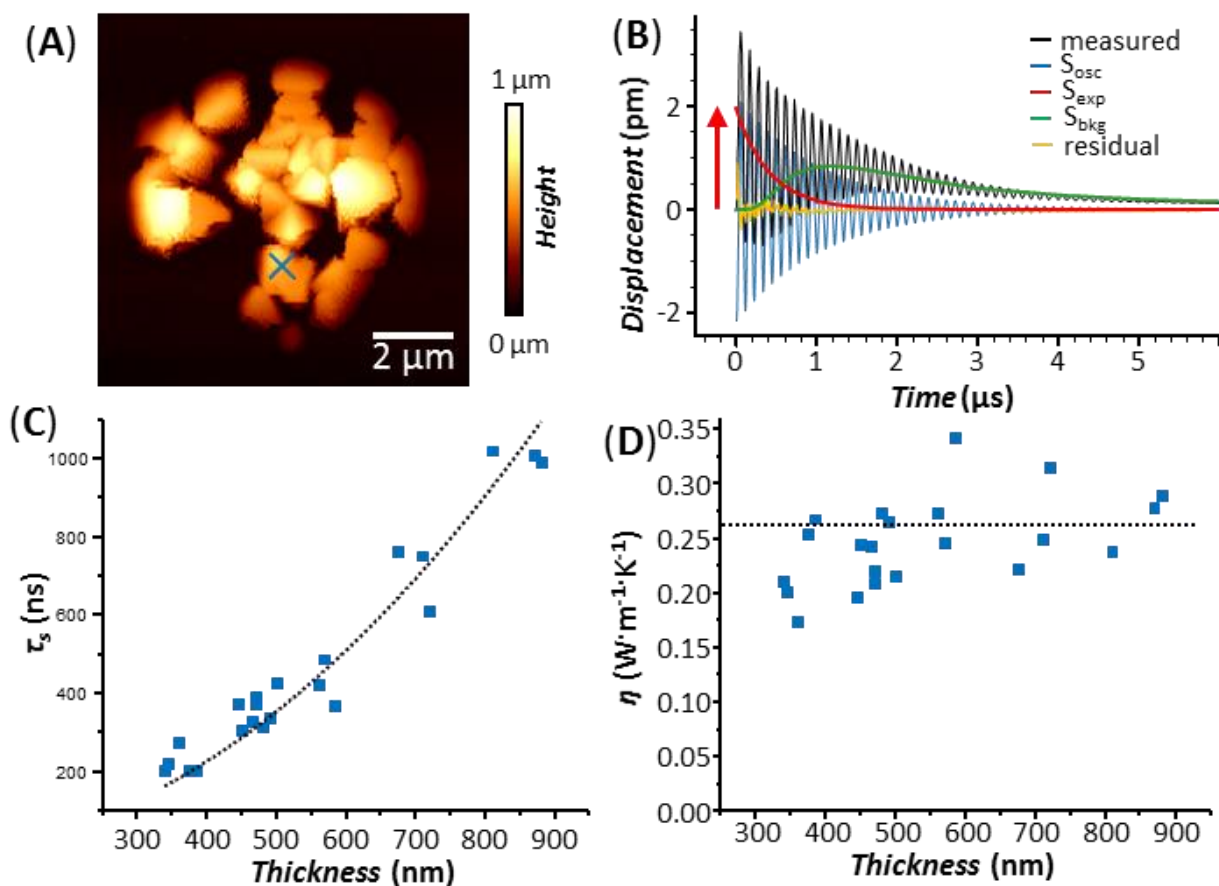**Fig. 4. HKUST-1 metal organic framework microcrystals thermal conductivity measurement**. (**A**) AFM topography image of MOF microcrystals. (**B**) Transducer signal (1388 cm^{-1}) for 560 nm thick HKUST-1 microcrystal (x-label in panel A) showing positive thermal expansion (red). (**C**) thermalization time as a function of thickness; the black line is given by eq. 5. (**D**) HKUST-1 MOF thermal conductivity as a function of thickness.
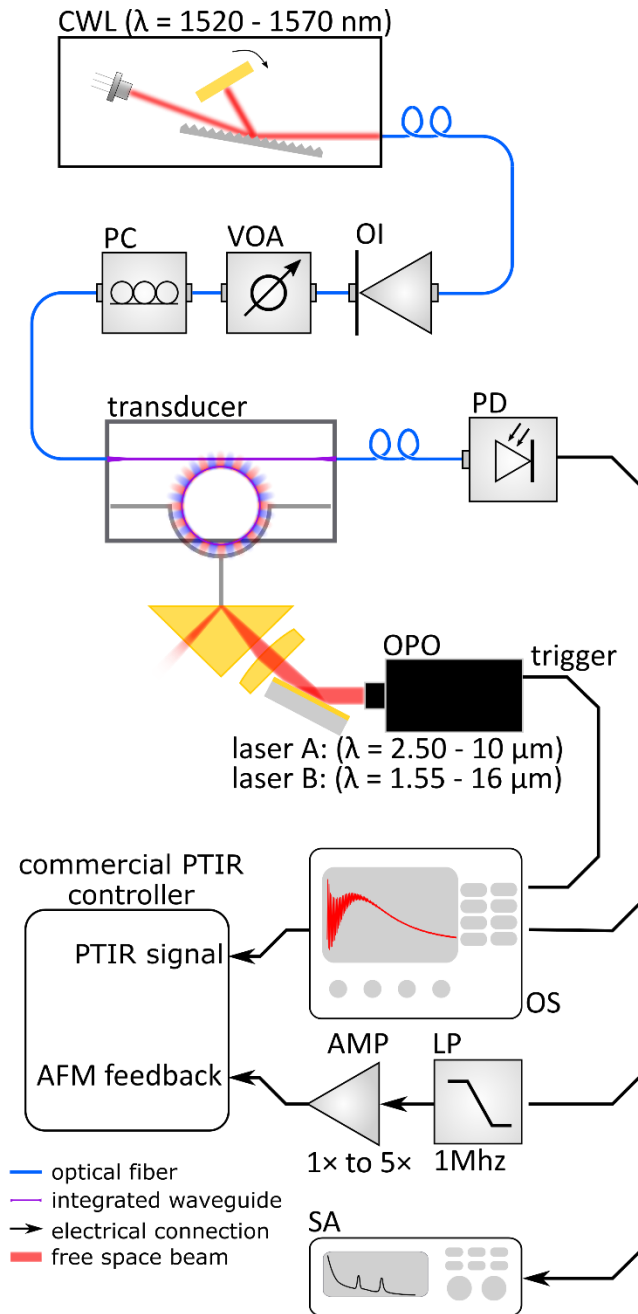
Fig. 5. PTIR measurement schematic with the transducers. Optics and electronics schematic that enable the integration of the optomechanical transducer probes with a commercial PTIR system. CWL: CW tunable diode laser, OI: optical isolator, VOA: variable optical attenuator, PC: polarization controller, PD: photo-detector, LP: low-pass filter, AMP: electronic amplifier, SA: spectrum analyzer (used for tip diagnostics and noise spectral density measurement), OS: high-speed oscilloscope, OPO: wavelength-tunable OPO pulsed laser source. Fiber based optical connections are drawn in blue, integrated waveguide structures are purple, electrical connections are black, free space optical beams are drawn in red.

ASSOCIATED CONTENT

Supporting Information. Methods Section including: transducers fabrication, sample preparation, data fitting procedure, supplementary discussions (SD1-7), Figures. S1 to S6, Tables S1 and S2.

AUTHOR INFORMATION

Corresponding Author

* Andrea Centrone andrea.centrone@nist.gov, Vladimir Aksyuk vladimir.aksyuk@nist.gov

Present Addresses

† Current address: Center for Quantum Nanoscience, Institute for Basic Science (IBS), Seoul 03760, Republic of Korea; Department of Physics, Ewha Womans University, Seoul 03760, Republic of Korea

§ Current address: Department of Physics and Astronomy, Seoul National University, Seoul 08826, South Korea.

Author Contributions

The manuscript was written through contributions of all authors. All authors have given approval to the final version of the manuscript. ‡These authors contributed equally.

REFERENCES

1.   Bao, W.; Melli, M.; Caselli, N.; Riboli, F.; Wiersma, D. S.; Staffaroni, M.; Choo, H.; Ogletree, D. F.; Aloni, S.; Bokor, J.; Cabrini, S.; Intonti, F.; Salmeron, M. B.; Yablonovitch, E.; Schuck, P. J.; Weber-Bargioni, A. *Science* **2012,** 338, 1317-1321.
2.   Centrone, A. *Annu. Rev. Anal. Chem.* **2015,** 8, 101-126.
3.   Rico, F.; Gonzalez, L.; Casuso, I.; Puig-Vidal, M.; Scheuring, S. *Science* **2013,** 342, 741-743.
4.   Ruggeri, F. S.; Longo, G.; Faggiano, S.; Lipiec, E.; Pastore, A.; Dietler, G. *Nat. Commun.* **2015,** 6, 7831.
5.   Lu, F.; Jin, M. Z.; Belkin, M. A. *Nat. Photonics* **2014,** 8, 307-312.
6.   Sahin, O.; Magonov, S.; Su, C.; Quate, C. F.; Solgaard, O. *Nat. Nanotechnol.* **2007,** 2, 507-514.
7.   Majumdar, A. *Annu. Rev. Mater. Sci.* **1999,** 29, 505-585.
8.   Laraoui, A.; Aycock-Rizzo, H.; Gao, Y.; Lu, X.; Riedo, E.; Meriles, C. A. *Nat. Commun.* **2015,** 6, 8954.
9.   Leblebici, S. Y.; Leppert, L.; Li, Y.; Reyes-Lillo, S. E.; Wickenburg, S.; Wong, E.; Lee, J.; Melli, M.; Ziegler, D.; Angell, D. K.; Ogletree, D. F.; Ashby, Paul D.; Toma, F. M.; Neaton, J. B.; Sharp, I. D.; Weber-Bargioni, A. *Nature Energy* **2016,** 1, 16093.
10.   Chen, J.; Badioli, M.; Alonso-Gonzalez, P.; Thongrattanasiri, S.; Huth, F.; Osmond, J.; Spasenovic, M.; Centeno, A.; Pesquera, A.; Godignon, P.; Zurutuza Elorza, A.; Camara, N.; de Abajo, F. J. G.; Hillenbrand, R.; Koppens, F. H. L. *Nature* **2012,** 487, 77-81.
11.   Katzenmeyer, A. M.; Holland, G.; Chae, J.; Band, A.; Kjoller, K.; Centrone, A. *Nanoscale* **2015,** 7, 17637-17641.
12.   Kouh, T.; Karabacak, D.; Kim, D. H.; Ekinci, K. L. *Appl. Phys. Lett.* **2005,** 86, 013106.
13.   Krause, A. G.; Winger, M.; Blasius, T. D.; Lin, Q.; Painter, O. *Nat Photon* **2012,** 6, 768-772.

14.   Wu, M.; Wu, N. L. Y.; Firdous, T.; Fani Sani, F.; Losby, J. E.; Freeman, M. R.; Barclay, P. E. *Nat. Nanotechnol.* **2017,** 12, 127-131.

15.   Srinivasan, K.; Miao, H.; Rakher, M. T.; Davanço, M.; Aksyuk, V. *Nano Lett.* **2011,** 11, 791-797.

16.   Dazzi, A.; Prater, C. B. *Chem. Rev.* **2017,** 117, 5146–5173.

17.   Dazzi, A.; Glotin, F.; Carminati, R. *J. Appl. Phys.* **2010,** 107, 124519

18.   Lahiri, B.; Holland, G.; Centrone, A. *Small* **2013,** 9, 439-445.

19.   Katzenmeyer, A. M.; Canivet, J.; Holland, G.; Farrusseng, D.; Centrone, A. *Angew. Chem. Int. Ed.* **2014,** 53, 2852-2856.

20.   Chae, J.; Dong, Q.; Huang, J.; Centrone, A. *Nano Lett.* **2015,** 15, 8114-21.

21.   Yang, J.; Ziade, E.; Schmidt, A. J. *Rev. Sci. Instrum.* **2016,** 87, 014901.

22.   Lee, J.; Farha, O. K.; Roberts, J.; Scheidt, K. A.; Nguyen, S. T.; Hupp, J. T. *Chem. Soc. Rev.* **2009,** 38, 1450-1459.

23.   Furukawa, H.; Cordova, K. E.; O'Keeffe, M.; Yaghi, O. M. *Science* **2013,** 341, 1230444.

24.   Huang, B. L.; Ni, Z.; Millward, A.; McGaughey, A. J. H.; Uher, C.; Kaviany, M.; Yaghi, O. *Int. J. Heat Mass Transfer* **2007,** 50, 405-411.

25.   Nandasiri, M. I.; Liu, J.; McGrail, B. P.; Jenks, J.; Schaef, H. T.; Shutthanandan, V.; Nie, Z. M.; Martin, P. F.; Nune, S. K. *Sci. Rep.* **2016,** 6, 27805.

26.   Katzenmeyer, A. M.; Holland, G.; Kjoller, K.; Centrone, A. *Anal. Chem.* **2015,** 87, 3154-3159.

27.   Ito, Y.; Virkar, A. A.; Mannsfeld, S.; Oh, J. H.; Toney, M.; Locklin, J.; Bao, Z. A. *J. Am. Chem. Soc.* **2009,** 131, 9396-9404.

28.   Choy, C. L. *Polymer* **1977,** 18, 984-1004.

29.   Yang, J.; Maragliano, C.; Schmidt, A. J. *Rev. Sci. Instrum.* **2013,** 84, 104904.

30.   Talin, A. A.; Centrone, A.; Ford, A. C.; Foster, M. E.; Stavila, V.; Haney, P.; Kinney, R. A.; Szalai, V.; El Gabaly, F.; Yoon, H. P.; Leonard, F.; Allendorf, M. D. *Science* **2014,** 343, 66-69.

31.   Zhuang, J.-L.; Ar, D.; Yu, X.-J.; Liu, J.-X.; Terfort, A. *Adv. Mater.* **2013,** 25, 4631-4635.

32.   Wu, Y.; Kobayashi, A.; Halder, G. J.; Peterson, V. K.; Chapman, K. W.; Lock, N.; Southon, P. D.; Kepert, C. J. *Angewandte Chemie International Edition* **2008,** 47, 8929-8932.

33.   Katzenmeyer, A. M.; Aksyuk, V.; Centrone, A. *Anal. Chem.* **2013,** 85, 1972-1979.

34.   Michels, T.; Rangelow, I. T.; Aksyuk, V. *Journal of Research of National Institute of Standards and Technology* **2016,** 121, 507-536.

35.   Chui, S. S. Y.; Lo, S. M. F.; Charmant, J. P. H.; Orpen, A. G.; Williams, I. D. *Science* **1999,** 283, 1148-1150.

36.   Gaur, U.; Lau, S.-f.; Wunderlich, B. B.; Wunderlich, B. *J. Phys. Chem. Ref. Data* **1982,** 11, 1065-1089.

37.   Wong-Ng, W.; Kaduk, J. A.; Siderius, D. W.; Allen, A. L.; Espinal, L.; Boyerinas, B. M.; Levin, I.; Suchomel, M. R.; Ilavsky, J.; Li, L.; Williamson, I.; Cockayne, E.; Wu, H. *Powder Diffr.* **2015,** 30, 2-13.

38.   Kloutse, F. A.; Zacharia, R.; Cossement, D.; Chahine, R. *Microporous Mesoporous Mater.* **2015,** 217, 1-5.

39.   Schoenecker, P. M.; Carson, C. G.; Jasuja, H.; Flemming, C. J. J.; Walton, K. S. *Ind. Eng. Chem. Res.* **2012,** 51, 6513-6519.

40.   Gomès, S.; Assy, A.; Chapuis, P.-O. *physica status solidi (a)* **2015,** 212, 477-494.

41.   Mills, G.; Zhou, H.; Midha, A.; Donaldson, L.; Weaver, J. M. R. *Appl. Phys. Lett.* **1998,** 72, 2900-2902.

42.   Bozec, L.; Hammiche, A.; Pollock, H. M.; Conroy, M.; Chalmers, J. M.; Everall, N. J.; Turin, L. *J. Appl. Phys.* **2001,** 90, 5159-5165.

Supplementary Materials for

Nanophotonic AFM Transducers Enable Nanoscale Chemical Composition and Thermal Conductivity Measurements at the Nanoscale

J. Chae,[1,2†§] S. An,[1,2†§§] G. Ramer,[1,2] V. Stavila,[3] G. Holland,[1] Y. Yoon,[1,2] A. Talin,[3] M. Allendorf,[3] V. A. Aksyuk[1]* and A. Centrone[1]*

Affiliations:

[1] Center for Nanoscale Science and Technology, National Institute of Standards and Technology, Gaithersburg, MD 20899, USA.

[2] Maryland Nanocenter, University of Maryland, College Park, MD 20742 USA

[3] Sandia National Laboratories, Livermore, CA 94551.

*Correspondence to: andrea.centrone@nist.gov, vladimir.aksyuk@nist.gov

†These authors contributed equally to this work

§ Current address: Center for Quantum Nanoscience, Institute for Basic Science (IBS), Seoul 03760, Republic of Korea; Department of Physics, Ewha Womans University, Seoul 03760, Republic of Korea

‡ Current address: Department of Physics and Astronomy, Seoul National University, Seoul 08826, South Korea.

This PDF file includes:

Methods

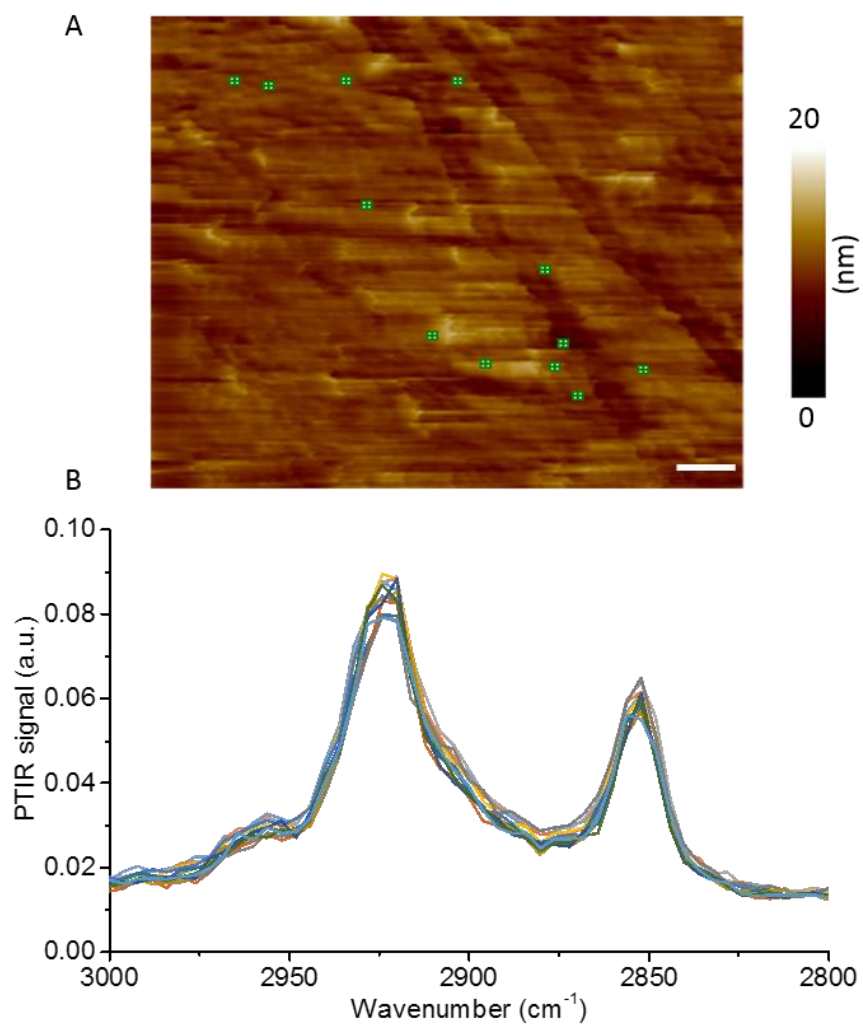Supplementary Text

Figs. S1 to S6

Tables S1 and S2

Fig. S1.

(A) Topographic AFM image of OTS self-assembly monolayer. Scale bar is 200 nm. (B) PTIR spectra obtained at different positions marked in panel-A. The typical signal-to-noise ratio (*SNR*) for a single spectrum (256 laser pulses per point) is ≈ 50.

Methods

All chemicals were used as received without further purification. The uncertainties throughout the manuscript represent a single standard deviation, unless otherwise noted.

<u>Optomechanical</u> <u>Transducers</u> <u>Fabrication</u>

The transducers were fabricated from a 260 nm thick single crystal silicon layer over a 1 μm thick buried oxide (BOX) layer of a silicon-on-insulator (SOI) chip. Typically, 16 transducers were fabricated on a single 3 cm × 3 cm square Si substrate. Fig S2 illustrate the nanofabrication process, which leverages electron-beam and multiple contact optical-lithography steps to define the device layers.

In the first step, electron-beam lithography (EBL) was used to define all the device features in the top Si layer, which was later etched by inductively-coupled plasma reactive ion etching with a C_4F_8 passivation-based SF_6 etching technique (Fig. S2A). Vertical and very smooth sidewall profiles are required to control the optical mode shapes and to obtain the high optical *Qs* that are necessary for achieving high transducer sensitivity and selectivity to the probe in-plane mechanical motion. In the fabrication, we paid particular attention to the narrow gaps and the small cantilever width, critical to transducer performance.

Low-pressure chemical vapor deposition (LPCVD) was used next to deposit SiO_2 and nitride layers (Fig. S2B). The oxide layer was used as optical cladding for the waveguide and as a sacrificial layer in the following fabrication. The nitride was later used as a mask layer for the hydrofluoric acid (HF) release step. Nitride windows near the microdisk/cantilever and the fiber couplers were opened by photolithography and reactive ion etching, as shown in Fig. S2C.

Next, the chip was annealed at 1000 °C for 1 h to densify and improve the film quality of the oxide and nitride layers. Subsequently, all layers were lithographically patterned and dry etched through to the substrate, followed by potassium hydroxide (KOH) anisotropic Si wet-etch to define the 75 μm deep v-grooves for the fiber optics and for the die separation via cleaving. During the KOH step, the transducer features and the inverse-taper optical couplers in the Si layer are sufficiently protected by the BOX and top oxide layers (Fig. S2D).

5 mm × 5 mm chips, each containing a single device, were mechanically cleaved. In each chip, the corner with the transducer was mechanically polished at 45° from the backside. At this point, a focused ion beam (FIB) was used to further undercut of the transducer area, exposing the AFM probe tip at the chip corner and to further sharpen the tip. This mechanical processing is needed to allow an unimpeded approach of the sample in the AFM experiments. (In the future this process may be accomplished by an appropriate combination of scalable back and front bulk micromachining techniques; a much more sophisticated process aimed at batch fabrication of a wide class of similar devices has been recently developed.[34] Finally, the devices are released by wet etching in a HF water solution (49 % mass fraction), followed by sequential rinsing in water and isopropyl alcohol and supercritical point drying.
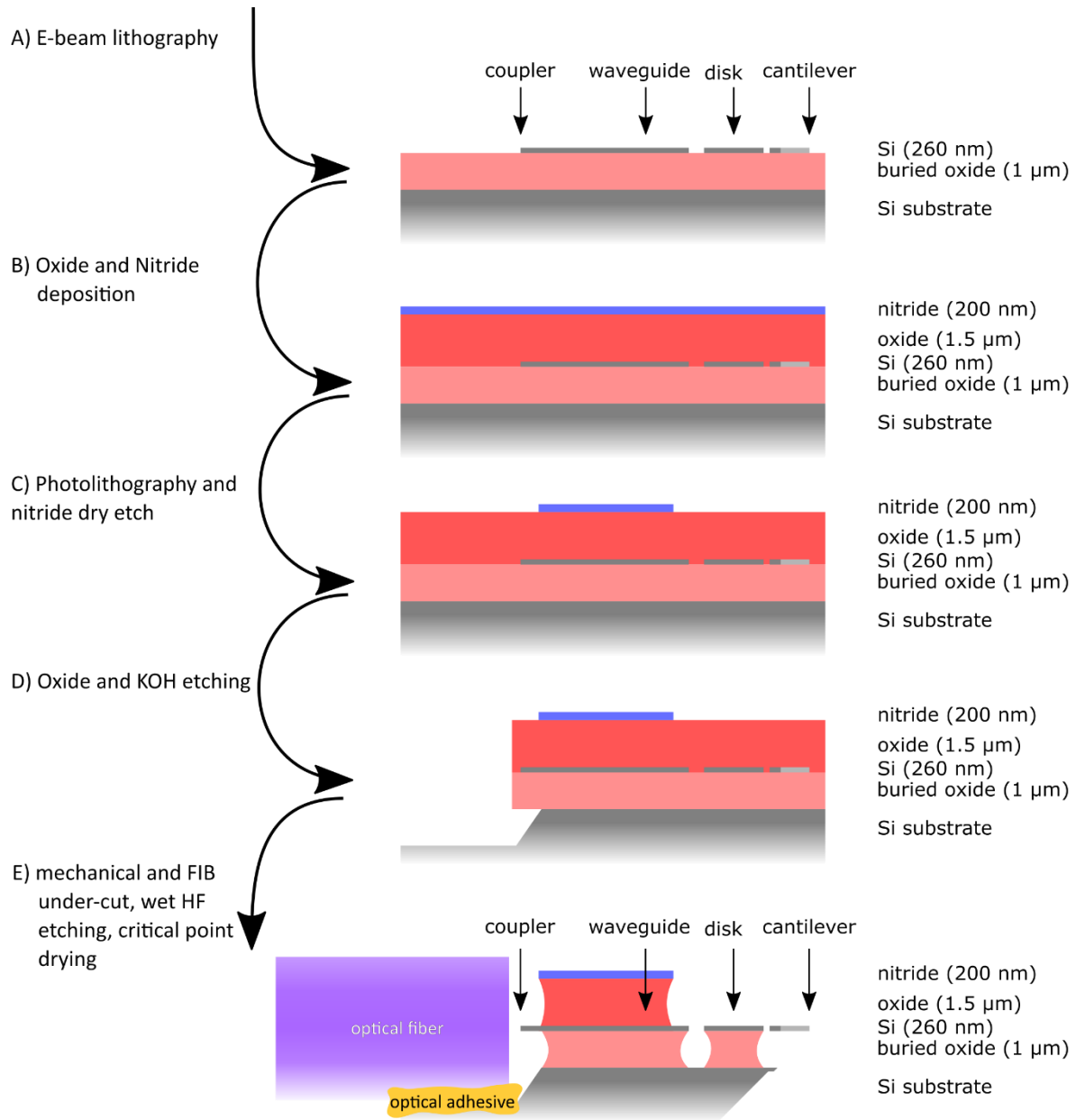
Fig. S2.

Transducer nanofabrication schematic (side view). (A) E-beam lithography patterning and etching of SOI Si layer. (B) Oxide & nitride depositions. (C) Photolithography and nitride dry etch (D) Photolithography patterning and etching of all surface layers and KOH V-grove etching. (E) Mechanical polishing and FIB under-cut of transducer probe tip and releasing with wet HF etching, critical point drying, and gluing

<u>Sample</u> <u>Preparation</u>

All ZnSe substrates (right angle prisms) were cleaned by ultrasonication in acetone (10 min) and rinsed with isopropyl alcohol followed by oxygen plasma cleaning (15 min).

a) *Heterogeneous polymer sample*:
Polymethylmethacrylate (PMMA) and polystyrene (PS) particles were embedded in an epoxy matrix. After hardening, the sample was microtomed into thin sections (300 nm $\pm$ 10 nm, as measured by AFM) and deposited on a ZnSe right angle prism.

b) *Octadecyltrichlorosilane (OTS) self-assembled monolayer*:
A 5 nm thick SiO_2 layer was deposited on the top surface of a ZnSe prism by electron beam evaporation. An OTS self-assembled monolayer was obtained on the SiO_2-coated prism top surface by immersing the prism in an OTS/toluene solution (5% volume fraction) for 1 h. The prism was then soaked in toluene for 1 h first and later in ethanol for 1 h. The substrate was finally dried with N2.

c) *PMMA wedge sample*:
PMMA (molecular weight, MW = 495000, 11 % mass fraction in anisole) was spin-coated ($\approx$ 33 Hz, for 1 min) on a ZnSe prism using a custom-made prism holder [18] and cured for 15 min at 150 ℃ to yield a $\approx$ 1 μm thick PMMA film. Later half of the film/prism was immersed in acetone for 10 min and rinsed with isopropyl alcohol to form a wedge in the proximity of the prism center. A representative topography profile of the PMMA wedge measured by AFM is shown in Fig. S3.
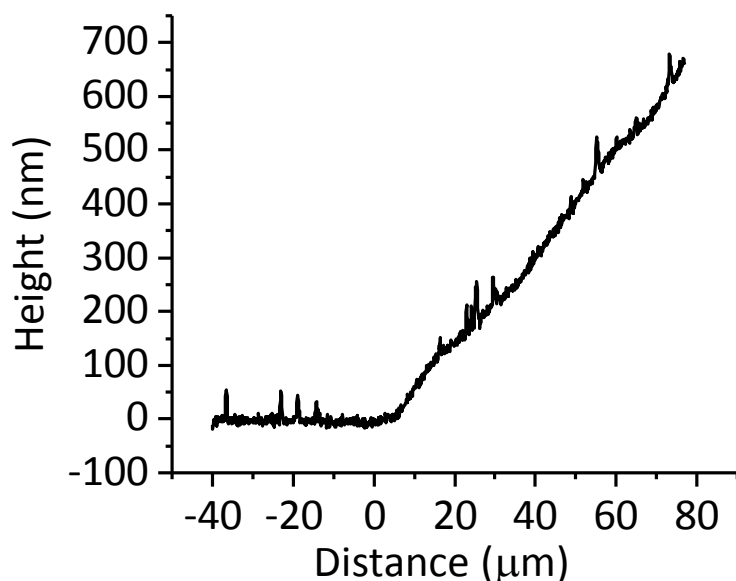

Fig. S3.
AFM height profile of the PMMA wedge sample.

d) *HKUST-1 microcrystals*:

Cu$_3$(BTC)$_2$·(H$_2$O)$_3$ (BTC, benzene-1,3,5-tricarboxylic acid), also known as HKUST-1 [30, 35], was deposited directly on a ZnSe prism by adapting a previously published ink-jetting procedure.[31] The HKUST-1 ink precursor solution was prepared by dissolving Cu(NO$_3$)$_2$·3H$_2$O (1.025 g) and BTC (0.507 g) in 6 mL of dimethyl sulfoxide (DMSO) by sonicating the mixture for 10 minutes at room temperature. The resulting solution was filtered through a 0.2 µm filter. Next, 2 mL of the precursor solution was added to a mixture of 4 mL ethanol and 3 mL ethylene glycol and sonicated for additional 10 minutes. The resulting ink was again filtered through a 0.2 µm filter prior to use. The HKUST-1 crystals were deposited directly on the surface of the ZnSe prisms using a commercial piezo-driven inkjet printer. After printing the desired patterns, the prisms were oven-dried in air at 90 °C for 2 minutes, washed in methanol, and then held in a covered Petri dish with methanol overnight.

PTIR data fitting procedure

Equations 1-4 in the main text were least-squares fitted to the time-domain PTIR trace data using the Levenberg-Marquardt nonlinear optimization algorithm. The data points corresponding to measurement times preceding the laser pulse were used to establish a constant baseline voltage that was subtracted from the trace. No other data pretreatment was done. Data points starting ≈ 4 ns after the beginning of the laser pulse were used for the fit. The free parameters were A, f, Q, B and τ_s. The f and Q values obtained from the fit are in good agreement with the values independently obtained from thermal noise power spectra (e.g. Fig 1G). The ratio of the DC amplitude to the AC amplitude (r, in Eq. 3) was held constant at 0.49, which is consistent with theoretical evaluation based on independently measured transducer parameters, described in SD-5. The sample-transducer distance x_t for calculating the thermal $S_{bkg}(x)$ was set to 12.5 µm, and 2.13×10^{-5} m^2/s was used for the air thermal diffusivity, as described in SD-6. Figs. 3A,B and 4B in the main text show representative fit curves for PMMA and HKUST-1 MOF, respectively.

As expected, we have observed close agreement between the contact mode frequencies and Qs measured in the independently acquired thermal noise spectra (Fig. 1G) and the frequencies and decay rates obtained via ringdown trace fits. This shows that we can understand PTIR signal with close to no adjustable parameters, other than overall signal amplitude, thermal background amplitude and the decay time τ_s, which is the focus of the measurement. Practically, f and Q in our fits were allowed to vary to produce the best possible oscillation signal match, but for a given series of experiments with the same probe we have kept r (SD5) and effective thermometer distance x_t (SD6) constant.

Calculation of the sample thermal conductivity, from the sample thermalization time and sample thickness

The thermal conductivity (η) of PMMA was calculated by fitting all the experimentally obtained τ_s values with equation 6 of the main text, leveraging literature data for the PMMA density (ρ) and heat capacity (C_p),[36] see table S1. In the fit, each experimental τ_s value was weighted by the inverse of its one standard deviation statistical uncertainty (shown in Fig 3C). The standard deviations were derived from repeat measurements obtained on distinct locations of the same thickness and

with different instrumental parameters such as excitation wavelength and pulse energy. The one standard deviation statistical uncertainty for the sample thickness (z) is estimated ± 5 nm from AFM measurements. For calculating the uncertainty (Δ) of η we have propagated the following relative uncertainties: $\Delta\rho = 5$ %, $\Delta C_p = 5$%, and the variance of the fit parameter of 3.5 % reported by the fit procedure. For PMMA, the statistical uncertainty $\Delta\eta = 8$ % is mostly determined by $\Delta\rho$ and ΔC_p.

The thermal conductivity of HKUST-1 microcrystals was calculated by fitting the experimentally obtained τ_s values with the simpler equation 5 of the main text. HKUST-1 ρ[37] and C_p,[38] in dry ($RH = 0$%) conditions were obtained from the literature, together with the known RH-dependent HKUST-1 water absorption isotherm,[39] to obtain $\rho(RH)$ and $C_p(RH)$, at $RH = 1.8$ % ± 0.3 % used in the experiments, see table S1. The HKUST-1 $\rho(RH)$ and $C_p(RH)$ values were obtained by assuming the MOF unit cell volume does not change with respect to the dry structure at the low RH observed in the experiments. ΔRH introduces a lower bound for $\Delta\rho \approx 1$ % and $\Delta C_p \approx 3$%. To calculate the HKIST-1 thermal conductivity, we used more conservative uncertainties values ($\Delta\rho \approx 2$ % and $\Delta C_p \approx 6$ %) to account for possible crystal to crystal variations due to defects.

For HKUST-1, the variance from the fit was ≈ 3 % and $\Delta\eta = 7$ % is mostly determined by ΔC_p.

Table S1.

Material properties used for calculating the sample thermal conductivity from PTIR data.

	ρ [kg·m^{-3}]	C_p [J/(kg·K)]	$\rho(RH=1.8\ \% \pm 0.3\ \%)$ [kg·m^{-3}]	$C_p(RH=1.8\ \% \pm 0.3\ \%)$ [kg·m^{-3}]
PMMA	1190 [36]	1368 [36]	-	-
HKUST-1	890 [37]	771 [38]	944 ± 009	968 ± 28

Supplemental discussion (SD) 1: comparison of transducer probes with temperature sensitive scanning thermal microscopy probes.

Scanning thermal microscopy (SThM)[7] is a well-established AFM technique that can qualitatively inform on the sample nanoscale thermal conductivity. However, despite lengthy tip-specific calibrations SThM hardly yields quantitative information because its dependence on the sample morphology.[40] Scanning thermal infrared microscopy (STIRM)[11] leverages nanofabricated SThM probes[41] and wavelength-tunable lasers to measures light-induced thermalization dynamic at the nanoscale to yield chemical composition and thermal conductivity (η) information without probe calibration. However, the slow response time of the SThM probe ($\tau_p \approx 15$ µs) limits such measurements to relatively thick (> 1.5 µm) samples with low η (< 0.2 W·m^{-1}·K^{-1}). Additionally the STIRM sensitivity and spatial resolution are typically one order of magnitude worse than for photothermal Induced Resonance (PTIR).[11] Essentially, to enable broad application, the STIRM measurement requires probes that are orders of magnitude more sensitive and have orders of magnitude faster response time (bandwidth) than SThM probes. However, the miniaturization of temperature sensitive AFM probes typically improves the sensor bandwidth at the expenses of its sensitivity.[11, 42] The transducers used in this work provide a paradigm shift for this measurement

thanks to both an improved signal-to-noise-ratio and a much wider bandwidth, that improves the probe response time by a factor of $\approx$ 1500 with respect SThM probes.[11] These characteristics greatly broaden the range of measurable samples with respect to the STIRM technique.

Supplemental Discussion 2: probe response signal to fast thermalization dynamics

Here we consider the excitation of the probe contact mode with modal stiffness k, contact modal mass m and angular frequency $\omega = \sqrt{k/m}$, by a short sample thermal expansion followed by rapid relaxation that occurs within a time $\tau_s \ll 1/\omega$. The mode is a dampened harmonic oscillator and the motion of the surface $x_{tip}(t)$ excites the mode by varying its instantaneous equilibrium position $x_0(t)$ in time: $x_0(t) = cx_{tip}(t)$, where the constant c is defined by the mode shape (for our probe $c \approx 1$, see SD 5).

The generalized force $F(t)$ acting on the mode generalized coordinate $x(t)$ is then given by:

$$F(t) = kx_0(t) = kcx_{tip}(t) \qquad (eqSD2.1)$$

During the short-lived force ($\tau_s \ll 1/\omega$), the mode, initially at rest, experiences acceleration $a(t) = k/m\,c\,x_{tip}(t) = \omega^2 c\,x_{tip}(t)$. We neglect the mode displacement during that time, because the probe does not appreciably move during the pulse.

The acquired velocity is

$$v = \int a(t)dt = c\omega^2 \int x_{tip}(t)dt \qquad (eqSD2.2)$$

The zero-to-peak modal amplitude x_{osc} can be obtained by transforming the acquired initial kinetic energy into potential energy

$$\frac{mv^2}{2} = \frac{kx_{osc}^2}{2} \qquad (eqSD2.3)$$

giving

$$x_{osc} = \frac{v}{\omega} = c\omega \int x_{tip}(t)dt \approx c\,\omega\,\langle x_{tip}\rangle\,\tau_s \qquad (eqSD2.4)$$

which shows that for a short-lived thermal expansion, $\tau_s \ll 1/\omega = 1/(2\pi f)$, the response (i.e. mechanical gain) is proportional to probe modal frequency. Consequently, in PTIR experiments on samples with rapid thermalization (i.e. thin samples or samples with high thermal conductivity) the high resonant frequency of the transducers ($f \approx$ 10 MHz) provides a large advantage relative to conventional cantilevers ($f \approx$ 200 kHz)

   Consistently with our analysis, the comparison of the PTIR signal obtained with a conventional cantilever to the signal obtained with a transducer on a 50 nm PMMA film under identical conditions, shows that the transducer improves the signal-to-noise ratio by $\approx$ 50 (Fig 1B, D). The transducer and the conventional cantilever here have approximately equal stiffness and therefore approximately equal root-mean-square thermal mechanical noise amplitudes, given by the equipartition theorem.

Supplemental Discussion 3: probe response noise in the frequency domain and probe response equipartition calibration

Figure S4 shows the measured noise spectral densities for a representative transducer, broken down by individual contributions. (The combined readout noise data is the same as in Fig. 1G in the main text). The mechanical, in-contact noise was obtained subtracting the separately measured readout noise power density from the total noise power density (corresponding to the traces in Fig 1G). The voltage noise power spectral density curves were measured by an electronic spectrum analyzer (left vertical axis) and converted to the input-referred displacement noise at the probe tip (right vertical axis) by using the equipartition theorem, as described below.

First, we modelled the device with a finite element method (FEM) where we adjusted the probe width to match the observed mechanical resonance frequencies for the probe oscillation modes, to obtain the DC stiffness of the probe of $k_{DC} \approx 1$ N/m. The deformation of the probe under a DC force applied to the tip can be described sufficiently well by the sum of the deformations of only the first 2 symmetric in-plane modes of the *free* probe (observed at ≈ 4 MHz and ≈ 14 MHz), because all other modes are very stiff in comparison. Correspondingly, the sum of the FEM modal stiffnesses (with tip displacement used as the mode generalized coordinate), $k_1 \approx 1.18$ N/m and $k_2 \approx 9$ N/m, account well for the DC response: $1/k_{DC} \approx 1/k_1 + 1/k_2$. The two modes have different optomechanical readout gains, that are separately estimated from the measured free probe noise spectral peaks (Fig. S4). The integrated voltage noise power from each Lorentzian peak $\langle V_{1,2}^2 \rangle$ is equated to $\langle x_{1,2}^2 \rangle = \frac{k_B T}{k_{1,2}}$ as expected per the equipartition theorem. The obtained modal readout gains are $g_1 \approx 30$ mV/nm and $g_2 \approx 45$ mV/nm. The resulting DC gain, due to the two transducing modes, is: $g_{DC} \approx k_{DC} (g_1/k_1 + g_2/k_2) \approx 30$ mV/nm.

The g_{DC} value depends on the specific measurement conditions, such as the CW output power of the fiber-coupled laser and the wavelength setpoint, however, a $g_{DC} \approx 30$ mV/nm is typical for the transduction gains. The gains are routinely recorded for each experiment using the AFM force curve, i.e. by applying a known tip displacement with the calibrated AFM z actuator. Notably, first mode contributes most (about 80 %) of the DC signal gain: $g_{DC,1} = k_{DC} g_1/k_1 \approx 25$ mV/nm ≈ 0.8 g_{DC}, because the second mode has a significantly higher stiffness and therefore responds less.

We use g_{DC} value to calibrate the vertical axis of Fig. 1G in the main text and right hand side vertical axis of Fig. S4, converting the voltage noise into the input-referred displacement noise. The measured readout noise spectral density is about 3 fm/Hz$^{0.5}$ at frequencies below contact resonance, i.e. for measurement bandwidths up to about 8 MHz.

The contact-resonance mechanical noise peak area adds input referred noise power of $\approx (20$ pm)^2 for measurement bandwidths above about 12 MHz. For example, a 10 ns measurement would have a noise equivalent bandwidth of $1/(4 \cdot 10$ ns$) = 25$ MHz, resulting in the combined input referred noise per point before averaging of ≈ 25 pm. For further noise reduction, most of the PTIR traces in our experiments are an average of 2048 individual pulse responses, and typically have

the statistical uncertainty of < 1 pm per point (at 10 ns per point), as suggested by this analysis. We note that we oversample the traces at 2 ns per point during data acquisition.

By increasing the fiber-coupled CW laser power, decreasing probe-disk gap or using higher Q optical modes, such transducers can achieve even better motion readout, ultimately limited by the optical shot-noise, rather than by the 'dark' photoreceiver noise. However, instead, the optical power, the probe-disk gap and the optical mode were chosen to maximize dynamic range and minimize frequency dependence of the readout gain, because in these conditions the probe already operates at only 3x the limit imposed by the very low mechanical probe off-resonance thermodynamic noise (Fig S4). The readout noise power is more than 20 dB below the mechanical noise power on resonance, and the thermodynamic noise is the dominant contributor for broadband measurement. Notably, further improvements are possible by simultaneously increasing the probe's stiffness and increasing the optical readout gain.

For completeness, based on k_{DC} and the free probe noise spectrum, we estimate that the thermodynamic (Langevin) force noise spectral density acting on a free probe is ≈ 5 fN/Hz$^{0.5}$ in air. This low in-air force noise is due to the small drag cross-section of the probe. Notably the probe remains thermodynamic noise limited (readout does not add appreciably to the input-referred noise) for frequencies from DC up to about 7 MHz.
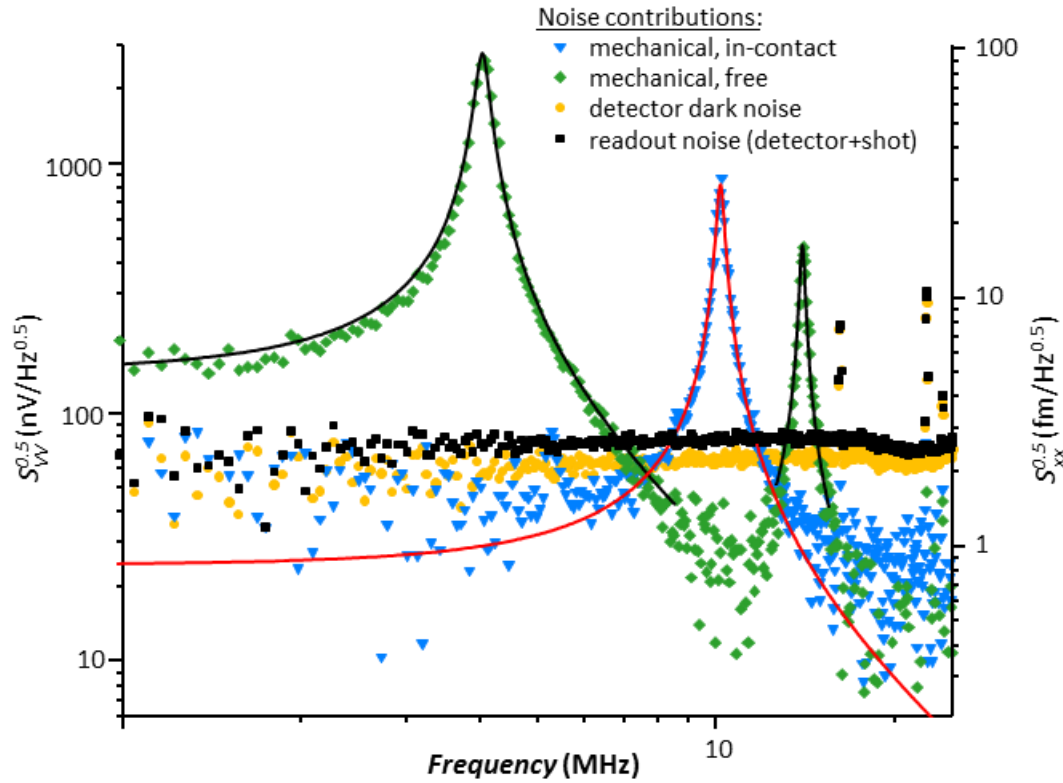

Fig. **S4**
Opto-mechanical transducer voltage and input-referred tip motion noise spectral density contributions. Harmonic oscillator fits to the probe modes (black line: free, red line: in contact)

are used for equipartition calibration of DC and contact mode opto-mechanical transduction (SD-3, SD-5)

Supplemental Discussion 4: Modelling of Thermalization dynamics

Here we use FEM calculations to show that the thermalization dynamics in the experiments are well described by single-exponential relaxation. The relaxation time scale τ_s is well approximated by the time constant of the fundamental thermal eigenmode (when the ZnSe substrate is modelled as a constant-temperature boundary condition). This result provides the basis for the application of equations 5 and 6 in the calculations of η from the experimentally determined τ_s values.

We use a one-dimensional FEM model because the PTIR laser spot size ($\approx$ 50 µm diameter) is much bigger than both the sample thickness (<1 µm) and the substrate thermal diffusion length during the few microsecond-long PTIR experiment. The model consists of a ZnSe substrate, the PMMA sample and air above the sample. The heat transport is diffusive only. The FEM calculation solves the diffusion equation

$$\rho C_p \frac{\partial u(x,t)}{\partial t} = \eta \frac{\partial^2 u(x,t)}{\partial^2 x} \qquad (eqSD4.1)$$

where, u is the temperature raise from equilibrium as a function of position (x) and time (t) through ZnSe, PMMA and air, ρ, C_p and η refer to density, specific heat and thermal conductivity of the three materials (see table S2).

Table S2.
Material properties used in the simulation.

	ZnSe	PMMA	Air
Thermal conductivity [W/(m·K)]	18	0.18	0.0257
Density [kg/m³]	5270	1180	1.2
Specific heat [J/(kg·K)]	339	1466	1005

The domain lengths of ZnSe and air in the model are set long enough (300 µm) to avoid possible artifacts from the boundary conditions. To mimic the impulsive laser heating of the sample, u in the calculation is changed from 0 at initial thermal equilibrium (before pulse) to $u(x, +0) = exp(-\frac{x}{l})$ for $0 < x < x_0$, inside the PMMA film. Because of the total internal reflection geometry used for the sample excitation, the light absorption profile that produces the initial localized heating is approximated by an exponential profile that decays away from the PMMA/ZnSe interface, Fig S5A (blue line). The decay scale $l \approx 500$ nm is based on the approximate optical penetration depth under total internal reflection illumination in our experiments.

The numerically calculated temperature profiles as a function of time are shown in Fig. S5A (colored lines). Although, for thick samples, the initial temperature profile in the system is highly non-uniform; for $t \geq 300$ ns, the temperature profile within PMMA is approximately $\propto$

$\sin\left(\frac{\pi}{2}x/x_0\right)$, which is the fundamental thermal mode shape in the film with fixed temperature at ZnSe interface $x = 0$ and zero heat flux at the air interface $x = x_0$. While heating of the ZnSe is apparent, it remains small. The decay rates of higher order thermal modes $\tau_m^{-1} = m^2\tau_s^{-1}$ increase quadratically with mode number m, which explains why the overall thermal relaxation can be approximated by the thermal relaxation of only the slowest, fundamental mode.

The temperature distribution u inside the PMMA film at any given time is used to calculate the PMMA thermal expansion as a function of time, (Fig. S5B) which is well fit by a simple single exponential decay $\propto e^{-t/\tau_s}$. The fit of the FEM-based thermal expansion relaxation for PMMA thicknesses ranging from 10 nm to 600 nm yields τ_s values that show a parabolic dependence of the PMMA thickness. From the parabolic best fit we find that these FEM-based decay rates are

$$\tau_s = 1.13\frac{4}{\pi^2}\cdot\frac{C_p\cdot\rho\cdot z^2}{\eta} \qquad \text{(eqSD4.2)}$$

Here the 13 % systematic discrepancy between the modeled values and the theoretical expression for the fundamental mode relaxation time is due to the combination of finite ZnSe heating and to higher-order mode contributions. We deem this accuracy acceptable for the benefit of obtaining simple analytic expressions describing our experiments, and note that more accurate analysis of measured high-fidelity thermal decay data is possible in future work based on either FEM models or more sophisticated theoretical treatment.
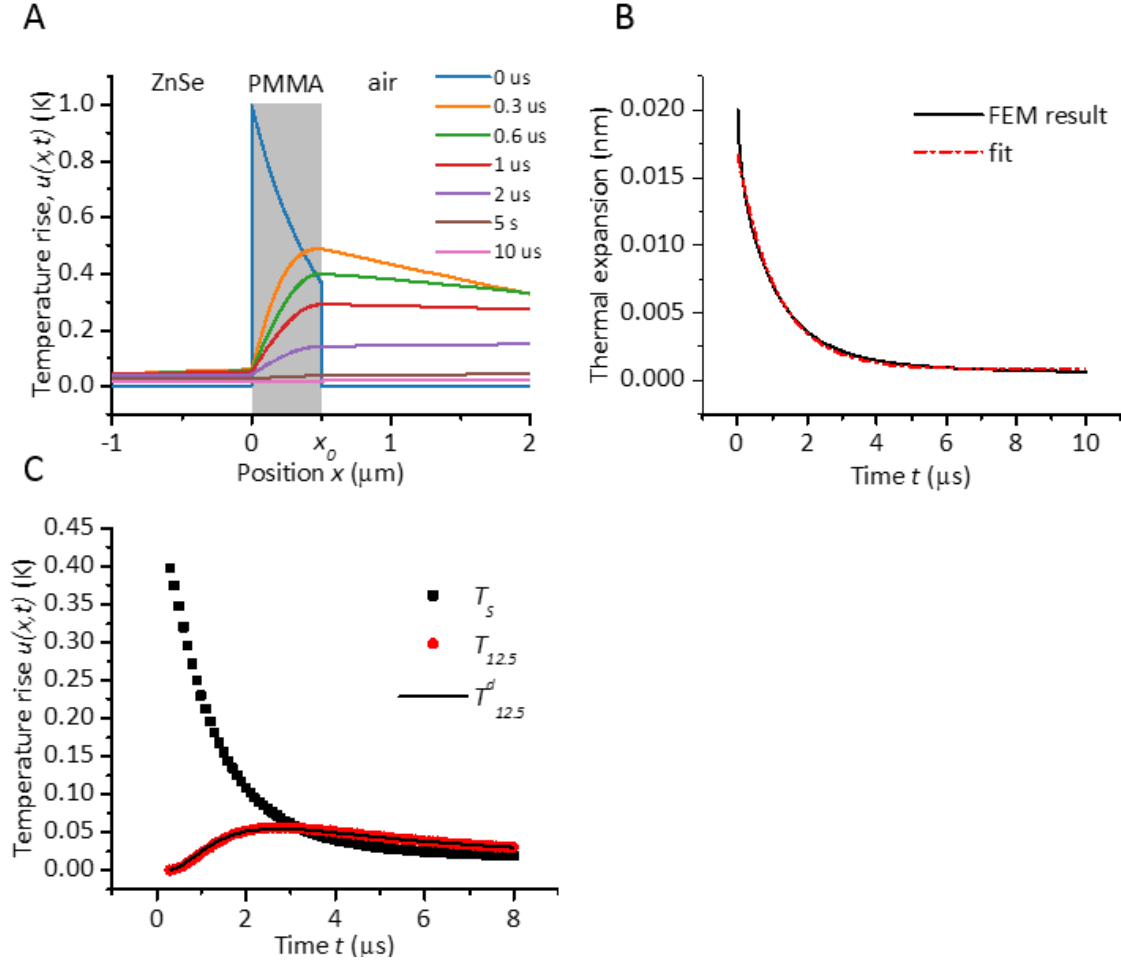
Fig. S5.
(A) Temperature profile across ZnSe, PMMA and air obtained by solving the diffusion equation. The black-line, at 0 µs, shows the initial temperature distribution expected from the absorbed optical energy density from a very short laser pulse. Temperature axis is scaled from 0 (initial thermal equilibrium temperature before the pulse) to 1 (maximum temperature at PMMA/ZnSe interface). Color lines at $t \geq 300$ ns show temperature distribution within PMMA and its time dependence that are well-described by considering only the fundamental thermal eigenmode in the film. The temperature change in ZnSe is minimal, because of the high thermal conductivity and heat capacity. (B) The time-dependent thermal expansion of PMMA derived from the temperature profiles inside the PMMA film is well described by a single exponential decay with a time constant approximately equal to that of the fundamental thermal eigenmode. (C) The temperature profile at the PMMA-air interface (T_S) and at 12.5 µm away from the surface ($T_{12.5}$) and the derived temperature profile ($T^d_{12.5}$) at 12.5 µm away from the surface temperature using the heat diffusion kernel and T_S.

Supplemental Discussion 5: Modeling of PTIR response ($S_{osc} + S_{exp}$)

To take full advantage of the high-bandwidth, high-SNR of the PTIR data provided by the transducers, here we carry out the exact analytic calculation of the mechanical components of the probe response ($S_{osc} + S_{exp}$). The calculation provides the exact phase for the decaying oscillation S_{osc}, the correct amplitudes of both signals and accounts for both the finite Q and for the short thermal decay time τ_s.

To describe the contact-resonance mode motion, we choose the mechanical displacement at the maximum-displacement location as the generalized coordinate x and use it for calculating modal stiffness and mass. We use finite element method to model the probe mechanics. We adjust the probe model geometry to match multiple resonance mode frequencies form FEM to the measured ones, and then calculate contact mode stiffness and the coefficient c (SD-2) between x_{tip} and the change in the modal coordinate's equilibrium value, $x_0 = c\, x_{tip}$. This is done by considering the boundary condition at the probe tip in contact with the sample as a massless spring and taking its high stiffness limit. For our probe geometry, we find $c \approx 1.0$. The optomechanical gain for contact mode g_{CM} is calculated using the equipartition theorem, based on a measured contact mode thermal noise peak and the numerically calculated modal stiffness.

We will assume an instantaneous expansion of the sample surface (short laser pulse relative to contact mode period) followed by exponential contraction back to the initial state with time constant τ_s. It is further assumed that the tip-sample stiffness is much higher than the probe stiffness and that the probe tip motion (x_{tip}) therefore follows the sample surface motion:

$$x_{tip}(t) = \theta(t)e^{-\frac{t}{\tau_s}}, \qquad\qquad (eqSD5.1)$$

where t is the time and $\theta(t)$ is a unit step function.
The mechanical PTIR response is a sum of 2 signals:
  (1) a 'DC' optomechanical signal due to the adiabatic change in the shape of the probe (the tip moves with the surface)
$$s_1(t) = g_{DC}x_{tip}(t) = g_{DC}\,\theta(t)e^{-t/\tau_s} \qquad\qquad (eqSD5.2)$$

  (2) and an 'AC' optomechanical transduction of the motion of the contact mode $x(t)$, relative to its time-varying equilibrium position $x_0(t)$,
$$s_2(t) = g_{CM}\big(x(t) - x_0(t)\big) \qquad\qquad (eqSD5.3)$$
Here g_{DC} and g_{CM} are optomechanical transduction gains for the static deformation (derived in SD-3) and the contact mode oscillation, respectively.

It is important to note that if the mode could deform adiabatically, i.e. tracking its time-varying equilibrium position, there would be no corresponding AC signal – because this would be already fully accounted for by the DC signal. The AC signal is thus proportional to the instantaneous *deviation* of the mode's generalized coordinate $x(t)$ from its equilibrium value $x_0(t) = c\, x_{tip}(t)$.

A simple, but useful limiting case of the mode's dynamic response is when the exponential decay time τ_s is much longer than the inverse of the mode's angular frequency (ω_0) that is, $\tau_s\omega_0 \gg 1$. In this limit, the mode vibration is excited by the initial instantaneous step in the surface position $\theta(t)$ and the subsequent adiabatic decay (e^{-t/τ_s}) does not modify the mode dynamics occurring near the mode resonance frequency. We also note that the mode typically has a high quality-factor $Q \gg 1$. Under these conditions the excited peak-to-peak vibration amplitude is then $x_{p-p} =$

$2x_0(t = +0) = 2c\, x_{tip}(t = +0)$, and the AC optomechanical signal is a simple ringdown given by

$$s_2(t) = -g_{CM}\, c\, \theta(t) e^{-\frac{\omega_0}{2Q}t} \cos \omega_0 t \qquad (eqSD5.5)$$

where g_{CM} is the mode's optomechanical gain and c describes the coupling between the tip displacement and the change in the mode's equilibrium position. We explicitly use a minus sign here to show that a positive instantaneous change in equilibrium position $x_0(t) = +\theta(t)$ produces an initial negative and equal mode displacement from equilibrium, $x(t = +0) = -1$.

Therefore, for this simple case the contributions (2) and (1) result in the transduction signal of the form:

$$S(t) = s_2(t) + s_1(t) = A\, \theta(t) \left(-\frac{1}{2} e^{-\frac{\omega_0}{2Q}t} \cos \omega_0 t + r e^{-t/\tau_s} \right) \qquad (eqSD5.6)$$

where $A \equiv 2g_{CM}c = 2|s_2(t = +0)|$ is the AC peak-to-peak amplitude, and r is the ratio of DC step to peak-to-peak AC amplitude, given by

$$r = \frac{s_1(t = +0)}{2|s_2(t = +0)|} = \frac{g_{DC}x_{tip}}{g_{CM}x_{p-p}} = \frac{g_{DC}}{2c\, g_{CM}} \qquad (eqSD5.7)$$

Calculating the right-hand side based on the results from the FEM model of the probe and measured noise power densities, we obtain $r \approx 0.48$, which closely matches with $r \approx 0.49$ obtained by fitting several PTIR traces with r as an adjustable parameter and averaging the resulting best fit values. This ratio is mainly the function of overall probe (and disk) shape and typically varies by less than 20 % even between probes of widely different stiffness ($> 2x$).

More generally, we now consider the mode response to an excitation with arbitrary τ_s (and Q). In this case, the motion equation is that of a harmonic oscillator with time-dependent instantaneous equilibrium position $x_0(t)$:

$$\ddot{x} + \frac{\omega_0}{Q}\dot{x} + \omega_0^2\big(x - x_0(t)\big) = 0$$

$$x_0(t) = c\, \theta(t) e^{-\frac{t}{\tau_s}} \qquad\qquad (eqSD5.7)$$

$$x(-\infty) = \dot{x}(-\infty) = 0$$

We first consider the impulse response of the mode – the mode response to an impulsive change in its equilibrium position $x_0(t) = \delta(t)$, where $\delta(t)$ is the Dirac delta function. Near t = 0 we have

$$\ddot{x} = \omega_0^2 x_0(t) = \omega_0^2 \delta(t) \qquad (eqSD5.8)$$

Therefore $\dot{x}(+0) = \omega_0^2$, while $x(+0) = 0$. The impulse response is $K(t) \equiv x(t) = \theta(t)\, \omega_0\, e^{-\frac{\omega_0}{2Q}t} \sin \omega_0 t$.

The solution of (eqSD5.7) is a convolution of $x_0(t) = c\, \theta(t) e^{-\frac{t}{\tau_s}}$ with the impulse response:

$$x(t) = \int_{-\infty}^{+\infty} x_0(\xi)\, K(t - \xi)\, d\xi = \int_{-\infty}^{+\infty} c\, \theta(\xi)\, e^{-\frac{\xi}{\tau_s}}\, \theta(t - \xi)\, \omega_0\, e^{-\frac{\omega_0}{2Q}(t-\xi)} \sin\big(\omega_0(t - \xi)\big)\, d\xi$$

$$= c\,\omega_0\,\theta(t)\int_0^t e^{-\frac{\xi}{\tau_s}}\,e^{-\frac{\omega_0}{2Q}(t-\xi)}\sin\big(\omega_0(t-\xi)\big)\,d\xi =$$

$$= c\,\theta(t)\frac{1}{\left(\frac{1}{\omega_0\tau_s}-\frac{1}{2Q}\right)^2+1}\left[e^{-\frac{t}{\tau_s}}+e^{-\frac{\omega_0}{2Q}t}\left(-\cos\omega_0 t+\left(\frac{1}{\omega_0\tau_s}-\frac{1}{2Q}\right)\sin\omega_0 t\right)\right]\quad (eqSD5.9)$$

We note again that the optomechanical signal consists of two parts,

$$S(t)=s_2(t)+s_1(t)=g_{CM}\big(x(t)-x_0(t)\big)+g_{DC}x_{tip}(t)=$$

$$= g_{CM}\big(x(t)-x_0(t)\big)+2r\,g_{CM}\,x_0(t)=\frac{A}{2c}x(t)+\frac{A}{2c}(2r-1)\,x_0(t)=$$

$$= \frac{A}{2}\,\theta(t)\frac{1}{\left(\frac{1}{\omega_0\tau_s}-\frac{1}{2Q}\right)^2+1}\left[e^{-\frac{t}{\tau_s}}+e^{-\frac{\omega_0}{2Q}t}\left(-\cos\omega_0 t+\left(\frac{1}{\omega_0\tau_s}-\frac{1}{2Q}\right)\sin\omega_0 t\right)\right]$$

$$+\frac{A}{2}\theta(t)(2r-1)e^{-\frac{t}{\tau_s}}\qquad\qquad (eqSD5.10)$$

Rewriting this expression by separating the oscillating and the exponentially decaying terms, we obtain equations 2 and 3 of the main text for $t>0$:

$$S(t)=S_{osc}(t)+S_{exp}(t)\qquad\qquad (eqSD5.11)$$

$$S_{osc}(t)=\frac{A}{2}\frac{1}{\left(\frac{1}{\omega_0\tau_s}-\frac{1}{2Q}\right)^2+1}e^{-\frac{\omega_0}{2Q}t}\left(-\cos\omega_0 t+\left(\frac{1}{\omega_0\tau_s}-\frac{1}{2Q}\right)\sin\omega_0 t\right)\quad (eqSD5.12)$$

$$S_{exp}(t)=A\left(r-\frac{1}{2}\frac{\left(\frac{1}{\omega_0\tau_s}-\frac{1}{2Q}\right)^2}{\left(\frac{1}{\omega_0\tau_s}-\frac{1}{2Q}\right)^2+1}\right)e^{-\frac{t}{\tau_s}}\qquad\qquad (eqSD5.13)$$

It is easy to see that in the previously considered limit of $\omega_0\tau\gg 1$, $Q\gg 1$ the full formula reproduces $(eqSD5.6)$.

Although we have used the full form of equations 2 and 3 in our data analysis, they could be considerably simplified without loss of accuracy. Typical in-contact Q factors for transducers in air are ≈ 20, therefore Q terms other than the exponential decay can safely be neglected for currently used probes:

$$S_{osc}(t)\approx\frac{A}{2}\frac{1}{\left(\frac{1}{\omega_0\tau_s}\right)^2+1}e^{-\frac{\omega_0}{2Q}t}\left(-\cos\omega_0 t+\left(\frac{1}{\omega_0\tau_s}\right)\sin\omega_0 t\right)\qquad (eqSD5.14)$$

$$S_{exp}(t) \approx A\left(r - \frac{1}{2}\frac{\left(\frac{1}{\omega_0\tau_s}\right)^2}{\left(\frac{1}{\omega_0\tau_s}\right)^2 + 1}\right)e^{-\frac{t}{\tau_s}} \qquad (eqSD5.15)$$

Considering the current probe frequency $\omega_0 \approx 2\pi \cdot 10$ MHz, the term $\frac{1}{\omega_0\tau_s}$ approaches unity only at extremely short decay times $\tau_s \approx 16$ ns. For longer τ_s timescales, it is reasonable to use perturbative expansion to the second order in the small parameter $\frac{1}{\omega_0\tau_s}$:

$$S_{osc}(t) \approx \frac{A}{2}\,e^{-\frac{\omega_0}{2Q}t}\left(-\left(1 - \left(\frac{1}{\omega_0\tau_s}\right)^2\right)\cos\omega_0 t + \left(\frac{1}{\omega_0\tau_s}\right)\sin\omega_0 t\right) \qquad (eqSD5.16)$$

$$S_{exp}(t) \approx A\left(r - \frac{1}{2}\left(\frac{1}{\omega_0\tau_s}\right)^2\right)e^{-\frac{t}{\tau_s}} \qquad (eqSD5.17)$$

Finally, we note that neglecting the Q terms may not be possible for the contemplated future transducer applications such as PTIR measurements in water or other viscous fluid, where the exact formulas derived above shall be used.

Supplemental Discussion 6: Origin of the non-mechanical signal

As the described in the main text, the PTIR response can be decomposed into three parts S_{osc}, S_{exp} and S_{bkg}. S_{osc}, S_{exp} are related to the mechanical motions of the nanoscale probe, as described in the main text and SD-5, S_{bkg} stems from non-local through-air heat transfer from the hot sample surface. The through-air heating shifts the optical resonance via the thermo-optic effect, i.e. the Si probe and disk refractive index changes as a function of its time-varying temperature (dn/dT ≈ 0.0002 K^{-1} near 1550 nm, T ≈ 300 K).

To understand the S_{bkg} origin and verify our interpretation we conducted a series of experiments on a ≈ 1 μm thick PMMA sample. The transducer probe was engaged on the sample surface, and the mid-IR tunable laser aligned in correspondence to the tip position (as typical in all PTIR measurements). In contact with the sample, S_{osc} is clearly visible in the PTIR signal (Fig S6A). The probe was then withdrawn and the PTIR signal measured at progressively increasing distances from the PMMA surface (Fig S6A and B). When the probe is not in contact with the sample, the PTIR signal is composed of the sum of an oscillating and of a background components, which both decrease in intensity as the probe is retracted to longer distances. When not in contact with the sample the oscillating signal is due to the through-air acoustic excitation of the probe which vibrates at the free-standing probe frequency (e.g. ≈ 4 MHz for a typical probe, see Fig S4); the time delay of the oscillation onset increases linearly with the probe sample distance (Fig S6C) with the proportionality coefficient given by the speed of sound in air.

The background component weakens as a function of distance and peaks at increasingly longer times. As shown below, this behavior and the overall S_{bkg} shape are well explained by heat diffusion through air from the hot sample surface, which experiences a very fast temperature rise followed by a slower (exponential) decay.

We model the transducer probe as a point thermometer located at a distance (x) from the sample surface. We assume that at any given time (t) the transducer is in thermal equilibrium with the immediately surrounding air and the refractive index is a linear function of its temperature $T(x, t)$ which produces a linearly proportional PTIR background signal.

Given a sample's surface temperature $T(0,t) \propto e^{-t/\tau_s}$, the air temperature is obtained by a convolution with the fundamental solution (i.e. impulse response) in 1D:

$$\text{T}(x,t) \propto \int_0^t e^{-\frac{w}{\tau_s}} \frac{x_t}{(t-w)^{\frac{3}{2}}} e^{-\frac{x_t^2}{4\alpha(t-w)}} dw \qquad (eqSD6.1)$$

where α is the thermal diffusivity of air ($2.13\text{x}10^{-5}$ m^2/s).

The PTIR signals obtained at controlled distances are well fit by equation ($eqSD6.1$) (Fig. S6B) and, using x as free fit parameter, returns values that increase linearly as function of the set distance. The offset ($x_t \approx 12.5$ µm) at zero tip-sample distance is consistent with the geometry of the transducer (≈ 10 µm disk plus probe, see Fig 1E in the main text). The $x_t = 12.5$ µm offset value was used to fit all the PTIR signals obtained in contact with the sample.

Additionally, to corroborate our analysis, we used the FEM model to extract the temperature profiles at the PMMA surface ($T_s(t)$) and in air 12.5 µm away ($T_{12.5}(t)$) (Fig. S5C). The $T_{12.5}(t)$, which describes the thermal background signal (see SD-5) is well described by equation eqSD6.1.
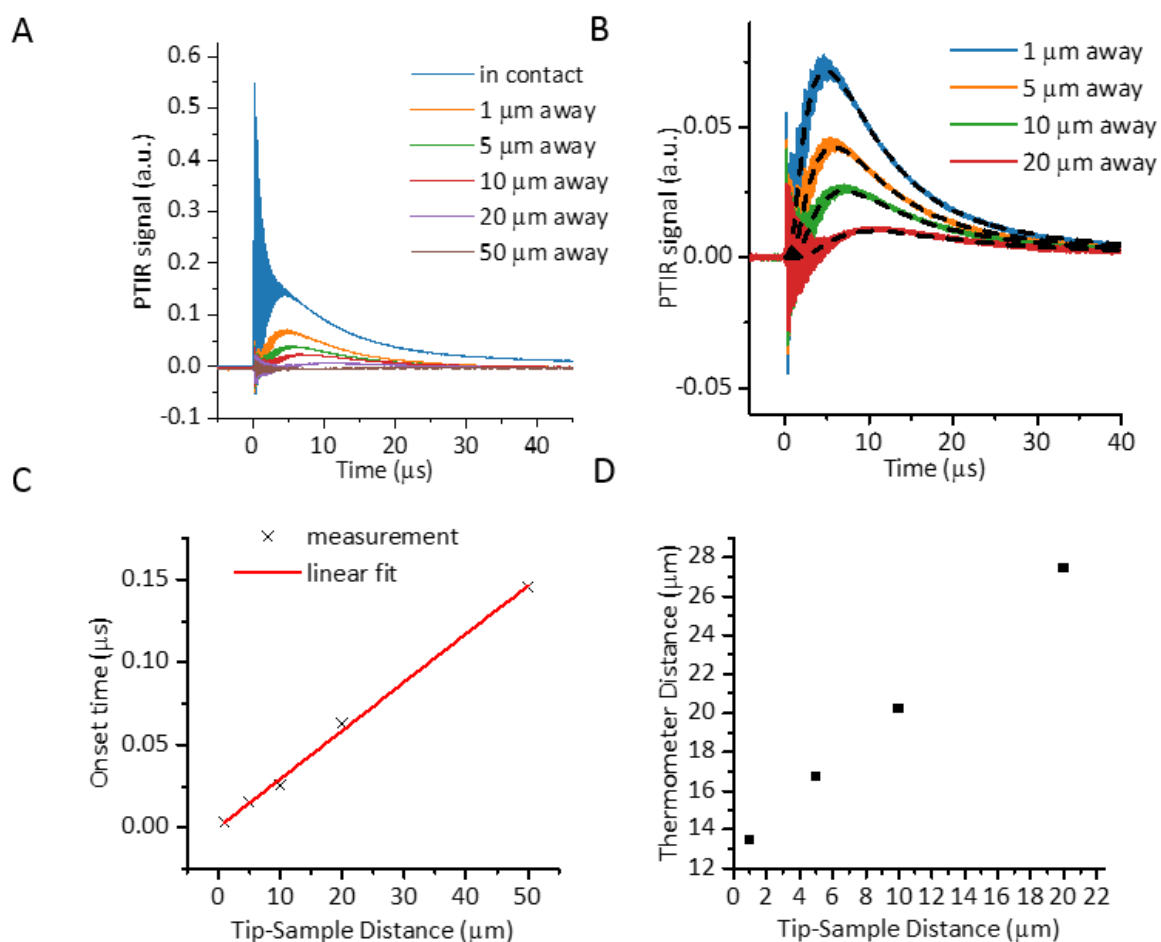
Fig S7.

(A) Measured PTIR responses for 1 µm thick PMMA in contact (black) and with the tip retracted at different distances. (B) Fitting of the background signal (black dashed lines) using heat diffusion through air. (C) The onset time of the PTIR oscillations as a function of the tip-sample distance. The delay is linearly proportional to distance and the propagation speed ($\approx$ 342 m/s) from the linear fit is consistent with the speed of sound in air at room temperature, as expected for acoustic excitation. (D) The thermometer distance obtained from the fits (C) as a function of the tip-sample distance. Horizontal axis distances are based on coarse positioning of the stepper motors, consequently the calibration between the number of steps and the absolute distance is approximate.

Supplemental Discussion 7: thermalization time as a function of R and η

Here we calculate the fundamental thermal mode of the heat diffusion equation in 1D:

$$\rho C_p \frac{\partial T(x,t)}{\partial t} = \eta \frac{\partial^2 T(x,t)}{\partial^2 x} \qquad (eqSD7.1)$$

in the presence of an interfacial thermal resistance R between the sample and the constant temperature substrate boundary (located at $x = 0$) and perfect thermal isolation on the other, sample-air boundary (located at $x = z > 0$).
Because of the low heat capacity and thermal conductivity of air, the heat flux through air is

$$j(z,t) = -\eta \frac{\partial T}{\partial x}(z,t) = 0 \qquad (eqSD7.2)$$

defining the boundary condition (BC).
The substrate is assumed to be at constant temperature, which without loss of generality, is chosen to be $T(-0,t) = 0$. In the absence of concentrated heat sources at the film/substrate boundary, the heat flux is continuous:

$$j(0,t) = -\eta \frac{\partial T}{\partial x}(z,t) = -R\,T(+0,t) \qquad (eqSD7.3)$$

which defines the other BC.
A mode has the form

$$T(x,t) = A\,e^{-t/\tau} \cos\left(\xi\left(1 - \frac{x}{z}\right)\right) \qquad (eqSD7.4)$$

which automatically satisfies the BC at $x = z$.
Using (eqSD7.1) and (eqSD7.3), we have:

$$\begin{cases} \dfrac{\rho C_p}{\eta}\dfrac{1}{\tau} = \left(\dfrac{\xi}{z}\right)^2 \\[2mm] \dfrac{\eta}{R}\dfrac{\xi}{z}\sin(\xi) = \cos(\xi) \end{cases} \qquad (eqSD7.5)$$

Defining $l_0 \equiv \eta/R$, we obtain

$$\begin{cases} \dfrac{\rho C_p}{\eta}\left(\dfrac{z}{\xi}\right)^2 = \tau \\[2mm] l_0 \dfrac{\xi}{z}\tan\xi = 1 \end{cases} \qquad (eqSD7.6)$$

or

$$\begin{cases} \dfrac{\rho C_p}{\eta}(l_0 \tan\xi)^2 = \tau \\[2mm] l_0 \xi \tan\xi = z \end{cases} \qquad (eqSD7.8)$$

which is eq. 6 of the main text.

The fundamental mode has $0 < \xi < \frac{\pi}{2}$, while generally for mode index m,

$$\pi(m-1) < \xi < \frac{\pi}{2} + \pi(m-1) \qquad (eqSD7.9)$$

notably, $\tau_m = \frac{\rho C_p}{\eta} \left(\frac{z}{\xi_m}\right)^2$ decreases slightly faster than quadratically with increasing m.

Supplemental Discussion 8: Laser repetition rate and PTIR throughput

Although, lasers operating at 1 kHz (1000 µs pulse spacing) such as the ones used in this work (see methods) offer broad tunability (from 400 nm to 16.0 µm)[26, 33] and are optimal in combination with conventional cantilevers (which relax back to equilibrium in ≈ 500 µs, Fig 1B), their repetition rate currently limits the transducers' PTIR throughput. We reason that leveraging wavelength-tunable quantum cascade lasers with narrower pulse spacing (i.e. 5 µs, 200 kHz) to match the relaxation time of our transducers (≈ 5 µs, Fig 1D) could further improve the PTIR throughput 200-fold.